The Stability of Arc Attachment in Arcjet Propulsion Devices

Submitted by:

Mark A. Cappelli
Benjamin Yuan
Mechanical Engineering Department
Stanford University
Stanford, CA 94305-3032

Submitted to:

Dr. Mitat Birkan
AFOSR/NA
110 Duncan Avenue, # B115
Bolling AFB DC 20332-0001

January, 1997

HIGH TEMPERATURE GASDYNAMICS LABORATORY
Mechanical Engineering Department
Stanford University

REPORT DOCUMENTATION PAGE

Form Approved
OMB No. 0704-0188

Agency reporting burden for this collection of information is estimated to average 1 hour per response, including the time for reviewing instructions, searching existing data sources, gathering and maintaining the data needed, and completing and reviewing the collection of information. Send comments regarding this burden estimate or any other aspect of this collection of information, including suggestions for reducing this burden, to Washington Headquarters Services, Directorate for Information Operations and Reports, 1215 Jefferson Davis Highway, Suite 1204, Arlington, VA 22202-4302, and to the Office of Management and Budget, Paperwork Reduction Project (0704-0188), Washington, DC 20503.

1. AGENCY USE ONLY (Leave blank)	2. REPORT DATE January, 1997	3. REPORT TYPE AND DATES COVERED Final Report

4. TITLE AND SUBTITLE The Stability of Arc Attachment in Arcjet Propulsion Devices	5. FUNDING NUMBERS F49620-93-1-0496

6. AUTHOR(S)

Mark A. Cappelli
Benjamin Yuan

7. PERFORMING ORGANIZATION NAME(S) AND ADDRESS(ES) Stanford University Mechanical Engineering Dept. Thermosciences Division Stanford, CA 94305-3032	8. PERFORMING ORGANIZATION REPORT NUMBER

9. SPONSORING / MONITORING AGENCY NAME(S) AND ADDRESS(ES) Air Force Office of Scientific Research 110 Duncan Ave., #B115 Bolling AFB, DC 20332-0001 *NA*	10. SPONSORING / MONITORING AGENCY REPORT NUMBER *93-1-0496*

11. SUPPLEMENTARY NOTES

12a. DISTRIBUTION / AVAILABILITY STATEMENT approved for public release; distribution is unlimited	12b. DISTRIBUTION CODE

13. ABSTRACT (Maximum 200 words)

The design of high current plasma devices such as arcjet thrusters, arc heaters, magnetohydrodynamic generators, and plasma opening switches has in the past been based mostly on empirical methods. In the case of arcjet thrusters, these methodologies have produced a steady, reliable device when operated at low power levels. However, it is desirable to increase the performance and operating range of the arcjet so that they may run more efficiently and reliably and be applicable to a wider set of missions

14. SUBJECT TERMS arcjet, modeling, electrodes, electric propulsion	15. NUMBER OF PAGES 88
	16. PRICE CODE

17. SECURITY CLASSIFICATION OF REPORT	18. SECURITY CLASSIFICATION OF THIS PAGE	19. SECURITY CLASSIFICATION OF ABSTRACT	20. LIMITATION OF ABSTRACT

The Stability of Arc Attachment in Arcjet Propulsion Devices

Submitted by:

Mark A. Cappelli
Benjamin Yuan
Mechanical Engineering Department
Stanford University
Stanford, CA 94305-3032

Submitted to:

Dr. Mitat Birkan
AFOSR/NA
110 Duncan Avenue, # B115
Bolling AFB DC 20332-0001

January, 1997

Table of Contents

Chapter 1. Introduction

1.1. Motivation

The design of high current plasma devices such as arcjet thrusters, arc heaters, magnetohydrodynamic generators, and plasma opening switches has in the past been based mostly on empirical methods. In the case of arcjet thrusters, these methodologies have produced a steady, reliable device when operated at low power levels. However, it is desirable to increase the performance and operating range of the arcjet so that they may run more efficiently and reliably and be applicable to a wider set of missions [1,2]. Because of the expense and time cost of empirical methods, attention has been turned to developing accurate numerical simulations which aspire to aid in the development of higher power designs, while providing a clearer understanding of internal physical processes. However, due to limitations in computing power and the complexity of plasma behavior, simplifications must be made to keep the calculations tractable.

It is well known that plasmas are an inherently unstable medium. Many steady state situations are precarious balances between competing mechanisms which can become unstable if those balances are slightly upset. The length and time scales over which these instabilities occur can be very small and difficult to capture in a larger scale simulation. Hence, much of the important smaller scale physics may not be captured by a computational model, resulting in an inability to capture real effects. In addition, the desire to calculate steady state solutions removes any ability to capture realistic time dependent phenomena. Existing codes [3-6] for arcjet simulation also impose a 2D, axisymmetric condition. These codes, while ambitiously trying to model the overall behavior of the arcjet, may not have the spatial or time dependent capabilities to capture small scale and asymmetrical effects. As a result, care must be exercised when interpreting the computed results for cases where there is no existing experimental data to compare with.

One phenomena that is sometimes seen during arcjet operation is the transition from a stable, diffuse mode of arc attachment on the anode to a destructive, spotty, and constricted attachment mode [7,8]. This phenomena is essentially an important limiting factor to the applicability of arcjets to more demanding space missions. A schematic of the arcjet running in the diffuse mode is given in Fig. 1.1. A possible cause of this transition is an instability which occurs in the near electrode region, much like the way instabilities in a laminar flow boundary layer lead to the transition to turbulence. These instabilities would in theory be initiated by small perturbations in plasma properties which grow in time. The purpose of this study is therefore to model the time dependent response of small oscillating disturbances in the near-anode region and to identify mechanisms which affect the growth or decay of these disturbances.
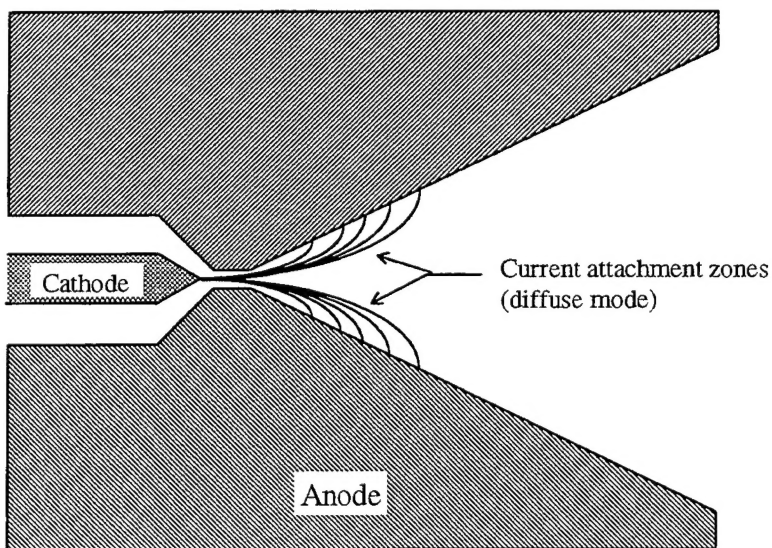
Figure 1.1. Cross section schematic of an arcjet running in the diffuse attachment mode.

The region near an anode in contact with a high pressure collisional plasma is characterized by a decrease in conductivity in relation to the far-field plasma because the anode acts as a catalyst to ion-electron recombination, and hence is a "sink" for charged particles. The charged particle density thus begins from a small value at the anode surface and increases to the value of the far-field plasma as the distance away from the

anode increases. This produces a small scale region where charged particle diffusion is driven by the gradients in the plasma properties. The plasma can be in a state of ionization in this region because of the depressed charged particle number densities. Due to the property gradients in this region, analogies can be made to the "fluid" and "thermal" boundary layers; hence the region is called the "electric boundary layer." At present, no arcjet model is believed to capture this region with sufficient accuracy and rigor. Several near-electrode models have been developed, however, which attempt to more completely capture the physics of this region by making simplifications in geometry and the regions outside the electric boundary layer [9-12]. Fig. 1.2 shows a schematic of the two general current attachment modes in a simplified planar anode geometry.
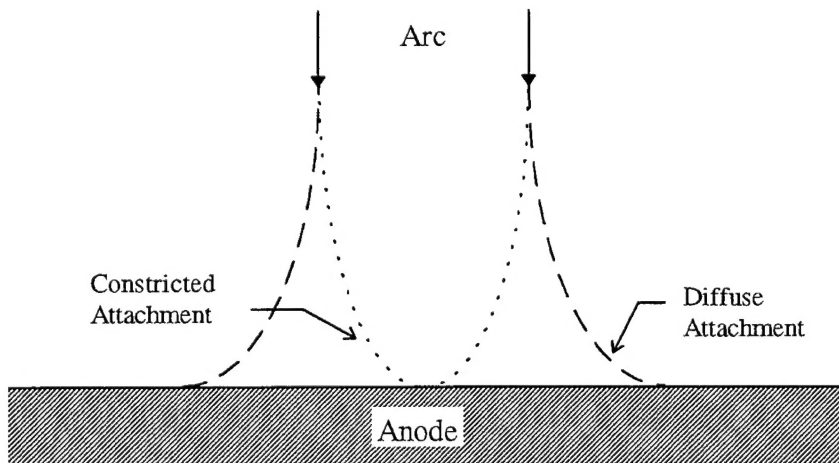
Figure 1.2. Schematic of the two attachment modes in a simplified planar geometry

1.2. Review of Relevant Studies

There have been a large number of studies performed on the transition from the diffuse to constricted anode attachment modes for vacuum arcs, but relatively few for the higher pressure cases. This is because of the historically large interest in increasing the reliability of triggered vacuum gaps and vacuum switches. It is instructive, however, to examine these studies to understand similarities and differences between the vacuum and

higher pressure cases. Despite the differences in operating pressures, there may be some similarities in the mechanisms of mode transition between vacuum and high pressure arcs due to phenomena (such as ionization and Joule heating) common to both cases.

In a vacuum arc, the sources of the interelectrode plasma are the electrodes themselves. The term "vacuum arc" is therefore a bit of a misnomer, since the gas near the electrodes can become collisionally dominated [13]. The current attachment process is separated into four different modes; the diffuse arc, footpoint, anode spot, and intense arc modes. At low current densities, the arc exists in the diffuse arc mode. In this mode the anode is basically inert, and acts as a collector of particles emitted from the cathode (ions, electrons, and atoms). There is no erosion at the anode and the voltage remains relatively low and quiet. Raising the current density may give rise to the footpoint mode, which is characterized by luminous spots and anode melting. This mode appears only under certain conditions, and sometimes may exist as an interim mode between the diffuse and anode spot modes. It is also usually accompanied by the appearance of arc noise (voltage fluctuations) and an increase in the mean arc voltage. These voltage fluctuations are associated with fluctuations in light intensity given off by the arc, which indicate that fluctuations in the electron number density and temperature [14] are occurring. The anode begins to take an active role in this discharge. The remaining two modes, which are associated with higher currents, are characterized by intense anode heating and erosion. The voltage is typically low and quiet in these modes. The anode acts as a copious source of vapor and ions, and has a temperature near the atmospheric boiling point of its material [13].

Many mechanisms have been postulated to be responsible for the transition of arc modes, as there has not been one mechanism identified which is exclusively responsible. These mechanisms include magnetic constriction in the plasma, as well as fluxes of material from the anode and cathode and thermal, geometric, and electrical effects of the anode. For example, some researchers contend that a significant anode vapor pressure, which is associated with higher anode temperatures, is a key requirement for transition.

Specifically, Wieckert and Egli [15] hypothesize that plasma production from ionization resulting from sufficient neutral number densities near the anode may provide the starting point for transition to an anode spot. Barinov and Smirnov [16] showed that anodes composed of materials whose erosion and ionization characteristics tended to produce greater densities of ions near the anode had correspondingly lower critical currents (the current at which an anode spot forms) than other electrode materials. Others have pointed out that the increase in voltage noise and magnitude at the moment of transition is due to the appearance of an ion- deficient region near the anode that creates a significant voltage drop, which can be on the order of the ionization potential of the plasma, due to the space charge [13]. The appearance of a rapidly oscillating voltage at transition also suggests the occurence of unstable phenomena [17]. Miller [13] has suggested that the most probable explanation of anode spot formation is a combination theory, in which many effects contribute in some way.

While the majority of research has been of an experimental nature, there have also been a few theoretical studies. One notable attempt was that of Ecker [18], who calculated critical current densities and anode temperatures for anode-spot transition. To make the calculations tractable, Ecker used a very much simplified one-dimensional model which assumed collisional dominance, local thermodynamic equilibrium, Saha equilibrium, and neglected inhomogenities, conduction losses, excitational energy losses and the sheath. Ecker found from his model that the transition was due to an instability which appears in the arc near the anode, and that a necessary but insufficient condition for the instability is the appearance of significant anode vaporization. His results exhibited some qualitative agreement (within an order of magnitude) and some differences with the available experimental data.

In contrast, there are far fewer studies which discuss mode transition for higher pressure arcs, where a gas takes on the role of the interelectrode plasma. It was mentioned in a review paper by Kimblin [19] that anode spot formation occurs at "short electrode spacings independent of the arc current" in the presence of an ambient gas.

This is because the gas shields the anode from the flow of ions from the cathode, creating an ion-deficient zone, which as discussed above is said to be a destabilizing influence, though many other factors also have an important effect. Dinulescu and Pfender [12] commented that the addition of a strong convective cathode jet also has a stabilizing affect; when electrode spacing was increased, the effect of the jet on the anode was reduced, which resulted in a mode transition at modest current densities.

Theoretical studies on the subject of atmospheric arcs have been in the form of steady state calculations of plasma properties [9-12]. From these studies, a better understanding of the structure of the anode sheath and non-equilibrium boundary layer was obtained. In particular, the past work of Self and Eskin [9], Cappelli [10], and Meeks and Cappelli [11] have helped clarify the physical processes and conditions distinguishing the diffuse and constricted modes of current attachment. In those studies, it was shown that for an anode in contact with a thermal plasma, the boundary layer voltage first increases with increasing current density, eventually reaching a local maximum. This point defines the demarcation between a positive and negative boundary layer impedance, where ionization within the electrical boundary layer is supported by increased ohmic heating. This current-voltage layer was found to be strongly influenced by the external flowfield. It was speculated that the regions of positive and negative boundary layer impedance correspond to the cases of diffuse and constricted modes of arc attachment. This contention, however, can only be confirmed or denied by a detailed unsteady analysis of the problem or by an experiment.

Other researchers have attempted to model the arc attachment process within the context of a practical device. For example, Paik et al [20] have applied the so-called Steenbeck Minimum Principle to a direct current (DC) discharge geometry often encountered in conventional arc plasma torches. They show that this principle, which is a special case of minimum entropy production, is useful in determining the position of the anode arc root in a plasma torch. They also find that the axial distance from the cathode tip to the steady state arc-root position decreases for increasing total current due to a

Okazaki et al [21,22] have made a serious attempt at theoretically understanding mode transition in an MHD generator. Their model identifies a parameter, defined as a ratio of Joule heat to conductive heat, which determines the stability of the boundary layers (electrical, thermal, and fluid). They conclude that a maximum value of this parameter exists which, when exceeded, leads to instability and hence mode transition. The analysis also relates stability characteristics to electrode temperatures, concluding that lowering the anode temperature, which lowers the conductivity of the adjacent plasma, reduces the critical current density at which mode transition takes place. Their model takes into account ionizational nonequilibrium and inhomogeneity in the plasma properties due to the boundary layer, but also makes some important simplifications. The plasma, which is formed from potassium-seeded combustion products, is assumed to have a perfect collisional coupling between the electrons and neutrals (though L.T.E is not assumed). Thus a simplified form of the electron energy equation, which balances inelastic collisional energy losses to Joule heating, is used, ignoring many other mechanisms of electron energy transfer such as convection, conduction, pressure work, and energy dissipation due to ionization.

It is clear from this review that the transition from diffuse to constricted current modes, which is seen in all regimes of plasma pressures, can be initiated by many different mechanisms. In the most general case, many phenomena, such as three dimensionality, unsteady behavior, bulk fluid flow, ion motion, ionizational non-equilibrium, electron energy conduction, surface effects, etc. should be accounted for. Simplifications must be made since this is clearly a monumental task. But as the old Taoist proverb goes, "A journey of a thousand miles begins with a single step."

1.3. Approach

In this thesis a theoretical analysis of the transient breakdown phenomenon in a high pressure plasma is presented and discussed. The approach used is to analytically examine the stability characteristics of the electrical boundary layer in a simplified planar geometry. This particular study is an extension of the work of Self and Eskin [9], which

introduces a model description for steady state current transfer from a planar electrode to a non-flowing thermal plasma. In this previous work, steady-state solutions of a simplified set of plasma conservation equations, which describe the characteristics of the one-dimensional electrical boundary layer, are obtained. The results of this study provide baseline profiles which are analyzed for their stability characteristics. From these results conditions which are favorable for instabilites to occur (and, we speculate, for the mode of current transfer to change) will be discussed and intuition about the effects of various physical mechanisms on stability will be developed. The model takes into account finite-rate ionization and recombination, the presence of an ambipolar field, pressure forces due to gradients in number density and temperature, collisional energy and momentum exchange, pressure work, inertia, and electron energy conduction and convection, many of which have been neglected in previous studies. Some important effects such as bulk fluid motion, heavy species thermal behavior, and multidimensionality are not included in the model for the sake of simplicity, though they should be included in future studies. Limitations of the model will become apparent and speculation on the effects of ignored processes will then be given.

Chapter 2. Model Description

The following 1-D continuum model is based on the equations derived by Eskin [9]. These equations are based on moments of the Boltzmann equation which describe the behavior of electrons and ions in a plasma. As stated in Eskin's thesis, the goal of this model is to examine the nature of the plasma-electrode interactions, and not to simply analyze one specific experiment or setup.

2.1. Governing Equations

The derivation of the governing equations which we will use, in their most general form, can be found in Appendix A of Eskin's thesis. It follows the standard methodology of taking moments of the Boltzmann equation for the ions and electrons in a weakly ionized plasma and making the usual heuristic descriptions of the collisional terms. For this study, the inertia terms in the momentum equations were kept to make the model applicable to a wider range of conditions; in addition, the unsteady terms were retained because of temporal nature of the investigation. The dependent variables are the electron and ion number densities, the electron and ion velocities, the electric field, and the electron temperature.

The set of equations describing the behavior of the electrons and ions are as follows:

Ion (j=i)and Electron (j=e) Conservation

$$\frac{\partial n_j}{\partial t} + \nabla \cdot \left(n_j \vec{V_j} \right) = \dot{n}_e = n_e n \alpha(T_e) - n_i n_e^{\ 2} \beta(T_e) \qquad (2.1.1)$$

Here, n_j and V_j represent the number density and velocity of species j (either electrons or ions), n represents the background neutral species density, $\dot{n}_e$ is the volumetric rate of ionization (for both the electrons and ions), and T_e is the electron temperature. We assume that electron collision-induced ionization and recombination dominate in the ionization and recombination process, and that $\beta(T_e)$ is the three body recombination coefficient given by Hinnov and Hirschberg [23]:

$$\beta(T_e) = 1.09 \times 10^{-20} T_e^{-\frac{9}{2}} \frac{m^6}{s} \tag{2.1.2}$$

For a weakly-ionized plasma, the ionization rate coefficient, $\alpha(T_e)$, is related to $\beta(T_e)$, the neutral temperature, T, and the pressure, P, through detailed balance:

$$\alpha(T_e) = \beta(T_e) n_{e_{eq}}^2 \left(\frac{kT}{P} \right) \tag{2.1.3}$$

Ion (j=i) and Electron (j=e) Momentum Conservation

$$n_j m_j \frac{\partial \vec{V}_j}{\partial t} + n_j m_j \left(\vec{V}_j \cdot \nabla \right) \vec{V}_j = -\nabla P_j + z_j e n_j \vec{E} - m_j n_j \vec{V}_j \nu_j \tag{2.1.4}$$

where $z_e = -1$, $z_i = +1$, e is the magnitude of the electron charge, $P_e = n_e k T_e$ and $P_i = n_i kT$ are the electron and ion pressures respectively, and ν_j is the electron or ion collision frequency with the background gas (related to the corresponding electron and ion mobility $\mu_j = e/m_j\nu_j$). We have neglected collisions between charged particles because of the assumed weakly ionized condition, the momentum transferred to the bath of electrons and ions due to the finite rate of ionization/recombination, and shear stresses.

Electron Energy

$$\frac{3}{2}n_e k \frac{\partial T_e}{\partial t} + \frac{3}{2} kn_e \vec{V}_e \nabla T_e + \nabla \cdot \vec{q}_e + P_e \nabla \vec{V}_e - m_e \nu_{en} \vec{\Gamma}_e \cdot \vec{V}_e = 3\delta_h \frac{m_e}{m} \nu_{en} n_e k(T - T_e) - \varepsilon_I \dot{n}_e$$

(2.1.5)

Here m is the mass of the background neutral species, δ_h is the nonelastic electron energy loss factor, which is much greater than unity only for molecular plasmas [24], and ε_I is the ionization energy of the neutral species. We have neglected work on electrons by shear stresses.

Poisson's Equation

$$\nabla \cdot \vec{E} = \frac{e}{\varepsilon_o}(n_i - n_e)$$

(2.1.6)

where ε_o is the permitivity of free space (8.854×10^{-12} Farads/m).

The heavy species (ions, neutrals) are assumed to be efficiently coupled, and therefore share the same uniform temperature, T, which removes the need for a global energy equation. The total pressure, P, is determined from the equation of state:

$$P = (n_e + n)kT + n_e kT_e \approx nkT$$

(2.1.7)

The electron and ion momentum equations are used to calculate the electron and ion velocities. The conduction current density can be calculated through the ancillary relation:

$$\vec{J} = \vec{J}_e + \vec{J}_i = en_e(\vec{V}_i - \vec{V}_e)$$

(2.1.8)

2.2. Assumptions

The additional assumptions which we use to further simplify the model to make the calculations more tractable are given as follows.   The independent spatial variable, x, describes the distance from the anode.

1.   A one dimensional system with a plane electrode contacting a semi-
infinite plasma in the half space $0 \leq x \leq \infty$, as shown in Fig 2.1.

Far-field Plasma

Current   Current

x

Planar Anode
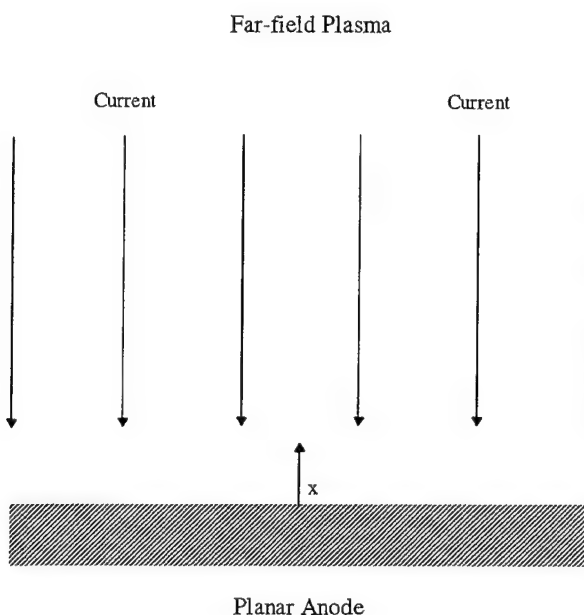
Figure 2.1. Schematic of the simplified, 1-D anode model.

2.   Ions and background neutral particles are at the same uniform temperature.

3.   There is no external magnetic field, and such fields due to plasma currents
are neglected.

4.   A net current to or from the electrode is allowed, and is assumed to be due
to an applied potential between the electrode and the distant plasma.

5.   The plasma is weakly ionized and quasineutral.

6.   There is no bulk fluid flow.

By invoking quasineutrality, it is implied that the scale length of the phenomena of interest is much larger than the Debye length, and that the frequency of any unsteady behavior is smaller than the plasma frequency. The requirement that heavy particles are at a constant uniform temperature is akin to assuming that the specific heat or conduction coefficient of the heavy species is infinitely large.

2.3. Non-Dimensionalization

To keep the model as general and simple as possible, all variables are non-dimensionalized by dividing them by reference parameters which correspond to the distant plasma conditions for the initially steady state one-dimensional electrical boundary layer. The reference parameters are defined in Table 2.1.

The variables are non-dimensionalized as follows:

$$\bar{t} = \frac{t}{t_R} \qquad\qquad \bar{x} = \frac{x}{l_R}$$

$$\overline{T}_e = \frac{T_e}{T_{e_R}} \qquad\qquad \overline{E} = \frac{E}{E_R}$$

$$\overline{n}_j = \frac{n_j}{n_R} \qquad\qquad \overline{\dot{n}}_e = \frac{\dot{n}_e}{\dot{n}_R} \qquad\qquad (2.3.1)$$

$$\widetilde{J} = \frac{J}{J_R} \qquad\qquad \overline{T} = \frac{T}{T_{e_R}}$$

$$\overline{U}_j = \frac{U_j}{l_R / t_R}, \text{ where } U \text{ is the x-component of the velocity vector } \overline{V}.$$

$$\overline{\Gamma}_j = \frac{\Gamma_j}{\Gamma_R}, \text{ where } \Gamma \text{ is the x-component of the flux vector } \vec{\Gamma}_j.$$

The non-dimensional set of equations which result from the substitution of these non-dimensional variables become:

Table 2.1. Reference Parameters for Non-dimensionalization

---

n_R : farfield, zero current, equilibrium electron number density

T_{e_R} : the zero current, distant plasma electron temperature $(=T)$

$\dot{n}_R = \beta\left(T_{e_R}\right)n_R^3$: the recombination rate in the distant plasma

$l_R = \sqrt{\dfrac{2D_a}{\beta\left(T_{e_R}\right)n_R^2}}$: the electron-ion recombination scale length

$\Gamma_R = \dfrac{2D_a n_R}{l_R} = n_R U_R$: the characteristic ambipolar flux

$E_R = \dfrac{kT_{e_R}}{el_R}$: the characteristic ambipolar field

$J_R = \sigma_R E_R$: the characteristic current density

$t_R = \dfrac{1}{\beta\left(T_{e_R}\right)n_R^2}$: the distant plasma characteristic recombination time

where

$\sigma_R = n_R e\left(\mu_i + \mu_e\right)$: the distant plasma electrical conductivity

$D_a = \dfrac{D_i\mu_e + D_e\mu_i}{\mu_e + \mu_i}$: the distant plasma ambipolar diffusion coefficient

$D_e = \dfrac{kT_{e_R}\mu_e}{e}$: the distant plasma electron free-diffusion coefficient

$D_i = \dfrac{kT_{e_R}\mu_i}{e}$: the distant plasma ion free-diffusion coefficient

---

Ion and Electron Conservation

$$\frac{\partial \overline{n}_e}{\partial \overline{t}} + \frac{\partial \overline{\Gamma}_j}{\partial \overline{x}} = \dot{\overline{n}}_e = \overline{n}_e \overline{T}_e^{-\frac{9}{2}}\left\{\overline{T}_e^{\frac{3}{2}}\exp\left[\overline{\varepsilon}_I\left(1 - \frac{1}{\overline{T}_e}\right)\right] - \overline{n}_e^2\right\}$$

(2.3.2)

where, for convenience, we have substituted $n_i = n_e$ from quasineutrality.

Subtracting the electron conservation equation from the ion conservation equation gives a simple relationship between the ion and electron flux:

$$\frac{d}{d\bar{x}}\left(\overline{\Gamma}_i - \overline{\Gamma}_e\right) = 0 \qquad (2.3.3)$$

or $J = J_{farfield} = constant$. This is a limitation of the 1-D quasineutral model which does not allow us to investigate the more general case of a non-zero perturbation in current density. It can be removed by expanding the model to include two-dimensional effects.

Electron Momentum Conservation

$$\frac{4}{(1+\mu)v_{in}t_R}\frac{m_e}{m_i}\overline{n}_e\left(\frac{\partial \overline{U}_e}{\partial \bar{t}} + \overline{U}_e\frac{\partial \overline{U}_e}{\partial \bar{x}}\right) = -\overline{n}_e\overline{E} - \frac{\partial \overline{n}_e\overline{T}_e}{\partial \bar{x}} - \frac{4\mu}{1+\mu}\overline{\Gamma}_e \qquad (2.3.4)$$

Ion Momentum Conservation

$$\frac{4}{(1+\mu)v_{in}t_R}\overline{n}_e\left(\frac{\partial \overline{U}_i}{\partial \bar{t}} + \overline{U}_i\frac{\partial \overline{U}_i}{\partial \bar{x}}\right) = \overline{n}_e\overline{E} - \frac{\partial \overline{n}_e}{\partial \bar{x}} - \frac{4}{1+\mu}\overline{\Gamma}_i \qquad (2.3.5)$$

Electron Energy Conservation

$$\frac{3}{2}\overline{n}_e\frac{\partial \overline{T}_e}{\partial \bar{t}} + \frac{3}{2}\overline{n}_e\overline{U}_e\frac{\partial \overline{T}_e}{\partial \bar{x}} + \overline{n}_e\overline{T}_e\frac{\partial \overline{U}_e}{\partial \bar{x}} - \frac{3}{5}\frac{1+\mu}{\mu}\frac{d}{d\bar{x}}\left(\overline{n}_e\overline{T}_e\frac{d\overline{T}_e}{d\bar{x}}\right) - \frac{4\mu}{1+\mu}\overline{\Gamma}_e\overline{U}_e = 3\theta\overline{n}_e\left(1 - \overline{T}_e\right) - \overline{\varepsilon}_I\overline{n}$$

$$(2.3.6)$$

The dimensionless parameters which we introduce in the electron energy equation are $\theta = \delta_H t_R e / m_i \mu_e$, the collision coupling factor, $\mu = \mu_i / \mu_e$, the ratio of ion and electron mobility, and $\bar{\varepsilon}_I = \varepsilon_I / kT_{e_R}$, the non-dimensional ionization energy

2.4. Stability Analysis

The stability of the electrical boundary layer is analyzed by modeling the time dependent effect of small oscillating perturbations in the plasma properties n_e, U_e, U_i, E, T_e which are superimposed on a set of steady state initial conditions. In keeping with our 1-D geometry, we assume that the perturbations are planar and hence propagate and vary in the x-direction only, perpendicular to the planar anode. Mathematically, each variable is decomposed into a component representing the steady solution and one representing the small perturbation as follows,

$$\bar{f}(\bar{x},\bar{t}) = \bar{f}_{ss}(\bar{x}) + \bar{f}'(\bar{x},\bar{t}) \tag{2.4.1}$$

where "f" denotes a plasma property such as n_e, U_e, U_i, E, T_e, and

$$\bar{f}'(\bar{x},\bar{t}) = \hat{\bar{f}}(\bar{x})e^{-i\bar{\omega}\bar{t}} \tag{2.4.2}$$

corresponds to a spatially varying temporally damped or growing oscillating perturbation. Here ω, which is in general complex, represents both the frequency of oscillation (real component) and growth (positive imaginary component) or decay (negative imaginary component) rate. The eigenfunction $\hat{\bar{f}}(\bar{x})$, which in general is also complex, describes the spatial amplitude as well as the phase relationships between the set of perturbation variables. There is no loss in generality by the use of this form for the disturbances because of the fact that arbitrary perturbations to linear systems, into which we can decompose our problem with a small amplitude approximation, can be decomposed into a

sum of fourier components. Each fourier component is represented by its frequency ω and can be analyzed independently from the others.

The focus of this study is to find situations where the imaginary component of ω, ω_i, is positive. This denotes a perturbation which is growing exponentially in time, and corresponds to a *linear instability*. Linear stability theory can determine whether there is an initial growth of a small disturbance, but cannot determine the behavior of that disturbance once its amplitude becomes large enough for non-linear effects to become important. As a result, linear stability theory does not guarantee that an unbounded growth is going to actually occur; however, because of the simplifications provided by using linear theory, it is often employed as a first step for gaining insight on the stability characteristics of physical situations.

To obtain the stability equations, equation 2.4.1 is substituted into the general equations 2.3.2 - 2.3.6 for each plasma property (n_e, U_e, U_i, E, T_e). Because the analysis is applied to known steady state solutions, terms which also appear in the steady state equations drop out. With the assumption that the perturbed quantities are very small compared to the steady state quantities, products of perturbed quantities can also be eliminated; the set is thus *linearized*. The remaining terms then form the following set of linear ordinary differential equations:

Particle Conservation

$$-i\omega\hat{\bar{n}}_e + \frac{d\hat{\bar{\Gamma}}_e}{dx} = \bar{T}_{e_{ss}}^{-3}\, exp\left[\bar{\varepsilon}_I\left(1-\frac{1}{\bar{T}_{e_{ss}}}\right)\right]\left[\hat{\bar{n}}_e + \frac{\bar{n}_{e_{ss}}}{\bar{T}_{e_{ss}}}\left(\frac{\bar{\varepsilon}_I}{\bar{T}_{e_{ss}}}-3\right)\hat{\bar{T}}_e + \frac{\bar{n}_{e_{ss}}^2}{\bar{T}_{e_{ss}}^{\frac{9}{2}}}\left[\frac{9}{2}\frac{\bar{n}_{e_{ss}}}{\bar{T}_{e_{ss}}}\hat{\bar{T}}_e - 3\hat{\bar{n}}_e\right]\right] = \hat{\bar{n}}_e$$

(2.4.3)

$$-i\omega\hat{\bar{n}}_e + \frac{d\hat{\bar{\Gamma}}_i}{dx} = \hat{\bar{n}}_e$$

(2.4.4)

Ion Momentum Conservation

$$\frac{4}{(1+\mu)v_{in}t_R}\left(-i\overline{\omega}\overline{n}_{e_{ss}}\hat{\overline{U}}_{e_{ss}}+\overline{U}_{i_{ss}}\frac{d\overline{U}_{i_{ss}}}{d\overline{x}}\hat{\overline{n}}_e+\overline{n}_{e_{ss}}\frac{d\overline{U}_{i_{ss}}}{d\overline{x}}\hat{\overline{U}}_i+\overline{n}_{e_{ss}}\overline{U}_{i_{ss}}\frac{d\hat{\overline{U}}_i}{d\overline{x}}\right)$$

$$=\overline{n}_{e_{ss}}\hat{\overline{E}}+\overline{E}_{ss}\hat{\overline{n}}_e-\frac{d\hat{\overline{n}}_e}{d\overline{x}}-\frac{4}{1+\mu}\left(\overline{n}_{e_{ss}}\hat{\overline{U}}_i+\overline{U}_{i_{ss}}\hat{\overline{n}}_e\right) \tag{2.4.5}$$

Electron Momentum Conservation

$$\frac{4}{(1+\mu)v_{in}t_R}\frac{m_e}{m_i}\left(-i\overline{\omega}\overline{n}_{e_{ss}}\hat{\overline{U}}_{e_{ss}}+\overline{U}_{e_{ss}}\frac{d\overline{U}_{e_{ss}}}{d\overline{x}}\hat{\overline{n}}_e+\overline{n}_{e_{ss}}\frac{d\overline{U}_{e_{ss}}}{d\overline{x}}\hat{\overline{U}}_e+\overline{n}_{e_{ss}}\overline{U}_{e_{ss}}\frac{d\hat{\overline{U}}_e}{d\overline{x}}\right)$$

$$=-\overline{n}_{e_{ss}}\hat{\overline{E}}-\overline{E}_{ss}\hat{\overline{n}}_e-\frac{d\overline{T}_{e_{ss}}\hat{\overline{n}}_e}{d\overline{x}}-\frac{d\overline{n}_{e_{ss}}\hat{\overline{T}}_e}{d\overline{x}}-\frac{4\mu}{1+\mu}\left(\overline{n}_{e_{ss}}\hat{\overline{U}}_e+\overline{U}_{e_{ss}}\hat{\overline{n}}_e\right) \tag{2.4.6}$$

Electron Energy Conservation

$$-\frac{3}{2}i\overline{\omega}\hat{\overline{T}}_e+\frac{3}{2}\left(\overline{U}_{e_{ss}}\frac{d\hat{\overline{T}}_e}{d\overline{x}}+\hat{\overline{U}}_e\frac{d\overline{T}_{e_{ss}}}{d\overline{x}}\right)+\hat{\overline{T}}_e\frac{d\overline{U}_{e_{ss}}}{d\overline{x}}+\overline{T}_{e_{ss}}\frac{d\hat{\overline{U}}_e}{d\overline{x}}-\frac{8\mu}{1+\mu}\overline{U}_{e_{ss}}\hat{\overline{U}}_e$$

$$-\frac{3}{5}\left(\frac{1+\mu}{\mu}\right)\left[\frac{1}{\overline{n}_{e_{ss}}}\frac{d}{d\overline{x}}\left(\overline{n}_{e_{ss}}\overline{T}_{e_{ss}}\frac{d\hat{\overline{T}}_e}{d\overline{x}}+\overline{T}_{e_{ss}}\frac{d\overline{T}_{e_{ss}}}{d\overline{x}}\hat{\overline{n}}_e+\overline{n}_{e_{ss}}\frac{d\overline{T}_{e_{ss}}}{d\overline{x}}\hat{\overline{T}}_e\right)-\frac{1}{\overline{n}_{e_{ss}}^2}\frac{d}{d\overline{x}}\left(\overline{n}_{e_{ss}}\overline{T}_{e_{ss}}\frac{d\overline{T}_{e_{ss}}}{d\overline{x}}\right)\hat{\overline{n}}_e\right]$$

$$=-3\theta\hat{\overline{T}}_e-\overline{\varepsilon}_I\frac{\exp\left(\overline{\varepsilon}_I\left(1-\frac{1}{\overline{T}_{e_{ss}}}\right)\right)\left(\frac{\overline{\varepsilon}_I}{\overline{T}_{e_{ss}}}-3\right)}{\overline{T}_{e_{ss}}^4}\hat{\overline{T}}_e-\frac{9}{2}\overline{\varepsilon}_I\frac{\overline{n}_{e_{ss}}^2}{\overline{T}_{e_{ss}}^{\frac{11}{2}}}\hat{\overline{T}}_e+\frac{2\overline{\varepsilon}_I\overline{n}_{e_{ss}}}{\overline{T}_{e_{ss}}^{\frac{9}{2}}}\hat{\overline{n}}_e \tag{2.4.7}$$

This set of equations describes the spatial variation of the perturbations $\hat{\overline{f}}(\overline{x})$ with distance from the electrode, and are subject to appropriate homogeneous boundary conditions at the far-field plasma and anode surface. These boundary conditions will be discussed in the next section. The actual solution to this set of equations is obtained by

solving a generalized eigenvalue problem, where $\bar{\omega}$ is the eigenvalue and the perturbation amplitudes $\hat{\bar{n}}_e, \hat{\bar{U}}_e, \hat{\bar{U}}_i, \hat{\bar{E}}, \hat{\bar{T}}_e$ form the eigenvector.

2.5. Boundary Conditions

Equations 2.3.2 - 2.3.6, without their unsteady terms, are a sixth-order, coupled, nonlinear set of partial differential equations. Six boundary conditions are therefore required for their steady-state solution, with 5 initial conditions additionally required for the unsteady problem. For the stability analysis, the steady state solution acts as the initial condition. Because of this, the solution of the steady problem is considered first.

In the farfield plasma, which we assume to be uniform, the four boundary conditions are found via the solution of the following set of algebraic equations:

$$\bar{n}_{e_\infty} = \bar{T}_{e_\infty}^{\frac{3}{4}} \sqrt{\exp\left(\bar{\varepsilon}_I\left(1 - \frac{1}{\bar{T}_{e_\infty}}\right)\right)} \tag{2.5.1}$$

$$\bar{E}_\infty = \frac{\bar{J}}{\bar{n}_{e_\infty}} \tag{2.5.2}$$

$$\bar{T}_{e_\infty} = 1 + \frac{1+\mu}{4\mu} \frac{\bar{E}_\infty \bar{J}}{3\theta \bar{n}_{e_\infty}} \tag{2.5.3}$$

$$\bar{\Gamma}_{i_\infty} = \frac{1+\mu}{4} \bar{J} \tag{2.5.4}$$

$$\bar{\Gamma}_{e_\infty} = -\frac{1+\mu}{4\mu} \bar{J} \tag{2.5.5}$$

The assumption that Saha equilibrium exists in the far-field region is the most convenient one possible, because it allows the far-field region to be uniform. In some devices, such as the arcjet thruster, the region far from the anode is not in ionizational equilibrium and hence is not uniform. For these cases, additional application specific

information is needed to formulate the far-field boundary condition. However, in order to keep the model as general and simple as possible, the assumption that equilibrium and uniform conditions exist in the farfield is utilized in this study.

For the stability analysis, all perturbations are set to zero in the far-field. This enforces the condition that the disturbances are not felt far away from the anode. In other words, the disturbances are assumed to originate in the electric boundary layer and die off away from the anode. Another possibilty is to assume a constant amplitude oscillation in the far-field region; this, however, can imply that disturbances are originating away from the anode and propagating towards it. There is also the possibility that these two boundary conditions represent the same disturbance. For example, a perturbation whose amplitude settles to a zero gradient in the far-field region may also be settling towards a zero value. For this study, it has been observed that both boundary conditions produce the same results.

2.6. Anode Surface Boundary Condition

Two additional boundary conditions are required at the anode for the steady state calculations. There have been many methods devised to model the way the plasma interacts with the anode. Some of these have been employed because of their mathematical simplicity. Examples of this are specifying the electron and ion number densities or fluxes at the anode. Although these representations may allow mathematical solutions for the problem, care must be exercised in the interpretation of results. Recently there have been attempts to use boundary conditions which possess more basis in physical reasoning. Examples of these methods are employing a unity sticking coefficient for electrons, modeling the emission characteristics of the electrode, and kinetic approaches. A more exhaustive review of the various methods which researchers utilized can be found in Meeks' thesis [11].

The difficulty in modeling the surface boundary condition is that the anode interacts in many different ways with the plasma. Meeks has come up with a fairly broad list of these interactions in her thesis, which include thermionic and secondary electron emission, ion-surface charge exchange, neutral-surface charge exchange, electron adsorption and the ability of the elctrode to capture or release "bulk" electrons contributing to current flow (where "bulk" refers to the solid electrode material). However, because the individual reaction rates for all these mechanisms are unknown, a global mechanism which takes the place of all these separate effects is used. This is implemented with an expression for the global surface reaction rate, which is postulated to have a first-order dependence on both the electron and ion densities as follows,

$$\overline{\Gamma}_i(\overline{x} = 0) = -k_{si}\overline{n}_e^2(\overline{x} = 0) \qquad (2.6.1)$$

where the quasineutral approximation has been applied. k_{si} is the reaction rate for the surface reaction represented by :

$$A^+ + e^- => A \qquad (2.6.2)$$

Although k_{si} is still unknown, it is only a single parameter and is thus much less cumbersome to deal with.

For the steady state solutions, the condition that

$$\frac{d\overline{T}_e}{d\overline{x}}(\overline{x} = 0) = 0 \qquad (2.6.3)$$

is used. This is the default boundary condition used in some arcjet models [4], and is also used in this study for consistency.

2.7. Approach to Solutions

The basic approach taken in this study is to:

1. Establish a baseline steady state solution methodology and results. The characteristics of the electrical boundary layer will be presented and reviewed.

2. Perform a simplified stability analysis based on a hypothetical uniform underdense plasma. The problem is greatly simplified while providing initial insight into the problem.

3. Extend the stability analysis to take into account the non-uniformity of the steady state electrical boundary layer. Here the most general case of this study is presented. Insights from the previous two sections are used and new information and insights are discussed.

Chapter 3.

Steady Behavior of the Electric Boundary Layer

We begin the study with the solution of the steady state equations which describe the background plasma in the stability analysis. The steady state equations are equations 2.3.2 - 2.3.6 without, of course, the unsteady terms.

3.1. Non-dimensional coefficients

Some insight into the character of these equations can be obtained by examining the constant coefficients in the equations. For example, by comparing the coefficient of the inertia term in the ion momentum equation with the coefficient of the collisional term, we see that if the product of t_r, the characteristic recombination time, and v_{in}, the ion-neutral collision frequency, is much larger than order 1, then the inertia term is insignificant in comparison with the collisional exchange term. Hence, under the higher pressure conditions for which this is true, collisional forces dominate. A similar argument can be made for the electron momentum equation, where we have the following condition for collisional dominance:

$$\frac{m_e}{m_i} \frac{1}{v_{in}} << \mu \tag{3.1.1}$$

The parameter θ determines how "collisionally coupled" the electrons are with the heavy species. Large values of θ denote situations of approximate thermal equilibrium between the electrons and heavy species, whereas small values denote less energy exchange and hence greater differences between the electron and heavy species' temperatures. Additionally, because of the assumption of a uniform heavy particle temperature, very high values of θ result in an isothermal condition for the electrons in this model.

3.2. Baseline conditions

To get an idea of what the magnitudes of the parameters θ, $\overline{\varepsilon}_I$, μ are in a real plasma of interest, we begin by examining the steady conditions which will become the basis for our stability analyses in this study. The situation we choose to model is the current attachment zone in a typical 1-kw arcjet thruster running on hydrogen. We again note that only a full multi-dimensional model can accurately capture the arcjet boundary layer profile, and that the results given here are intended to give qualitative insight and approximate behavior. Specifically, we additionally simplify the model by assuming that the plasma is 10% dissociated (i.e. the partial pressure of the dissociated atoms is 10% of the total pressure), and that the primary collisions are between electrons and hydrogen (H_2) molecules and dissociated hydrogen ions (H^+) and hydrogen molecules only. Charged particle collisions are thus ignored. Collisional cross section values are roughly estimated from the representitive data presented in Mitchner and Kruger [24]. Collisional frequency calculations involving the electrons are also based on the bulk temperature, which is a known parameter, rather than electron temperature, which must be calculated. The values for the parameters used are given in Table 3.1.

Equations 2.3.2 - 2.3.6 can now be solved given these parameters. The solution method we utilize in this study is based on a simple finite difference scheme which uses one-sided differences for first order derivatives and central differences for the second order derivatives. The discretized matrix is solved using a modified Newton-Raphson method present in the subroutine TWOPNT [26]. The results of the calculation provide the spatial profiles of $\overline{n}_e$, $\overline{U}_e$, $\overline{U}_i$, $\overline{E}$, $\overline{T}_e$, and $\overline{n}$ for a given current $\overline{J}$. For this study, results are given for three non-dimensional current densities of 0.4, 40, and 400. These correspond approximately to dimensional current densities of 10^2, 10^4, and 10^5 A/m^2, respectively.

We do not include the $\overline{J} = 4$ case because the boundary layer displays some unphysical characteristics in the current range from $\overline{J} \approx 2$ to $\overline{J} \approx 20$ for these conditions. The

Table 3.1. Property Values and Conditions for Baseline "Arcjet" Case

Gas	Hydrogen
Ionization energy	13.6 ev
Pressure, P	.5 atm
Bulk Temperature, T	6000 K
$\overline{Q}_{en}$	10^{-19} m^2
$\overline{Q}_{in}$	10^{-18} m^2
ν_{en}	2.94×10^{10} s^{-1}
ν_{in}	8.41×10^{9} s^{-1}
m_e	9.1095×10^{-31} kg
m_i	1.6744×10^{-27} kg $= m_H$
k_{si}	10^{15} cm^{4}mole^{-1}s^{-1}
δ_h	5
λ_d	1.33×10^{-6} m
n_{er}	1.61×10^{19} m^{-3}
t_R	.0356 s
l_R	.0289 m
E_R	17.9 N/C
$\dot{n}_R$	4.52×10^{20} m^{-3}s^{-1}
θ	2.85×10^{6}
$\overline{\varepsilon}_I$	26.3
μ	.0019

range of current densities for which this condition occurs depends upon the value of k_{si}. At the upper and lower limits of the range the ion flux is equal to zero at the anode boundary. At current densities within the saturation range, the calculated solution requires that the ion flux at the anode be positive. This phenomena, identified as *current saturation*, has been discussed in previous studies of steady state electric boundary layer

behavior [10,11]. It occurs for current densities in which the charged particles are not produced in sufficient quantities to satisfy a negative flux of ions to the anode. Because anodes are very poor ion emitters, a positive ion flux represents an unrealistic situation. The range of saturation is also affected by ε_p, the ionization energy of the gas. Gases with lower ionization energies tend to more easily supply the required ions to the anode and thus have smaller ranges of current saturation than those with higher ionization energies. We should also note that it is possible in such conditions for this phenomena to not appear at all.

3.3. Steady state profiles

The steady state profiles for the three current density cases are presented in Figs. 3.1 - 3.8. To maintain consistency between these figures, the $\bar{J} = 400$, 40, and 0.4 profiles are presented as a dashed line, a solid line, and a dotted line respectively. In order to show the profiles on the same plot, some figures, namely the electron number density and flux profiles, show profiles which have been normalized to their far-field values. Some curves are also displayed on specific length scales to better examine the particular regions of interest.

We begin the discussion with the results of the $\bar{J} = 0.4$ case. From Fig. 3.2, which shows the electron temperature profile, we see that the electrons are very nearly equilibrated with the heavy species. In fact, the electron temperature is actually slightly below the heavy species temperature near the anode. Fig. 3.3, which shows the electric field profiles, reveals that the field is actually negative in the boundary layer and hence impeding the flux of electrons toward the anode. Because of this, a "Joule cooling" of the electrons is occuring near the anode. At this low current density, the ambipolar field must impede the flow of electrons and ions because of the strong driving force provided by the pressure gradient. But despite these observations, the boundary layer remains in a state of ionization (though the ionization rates are very low compared to the other two
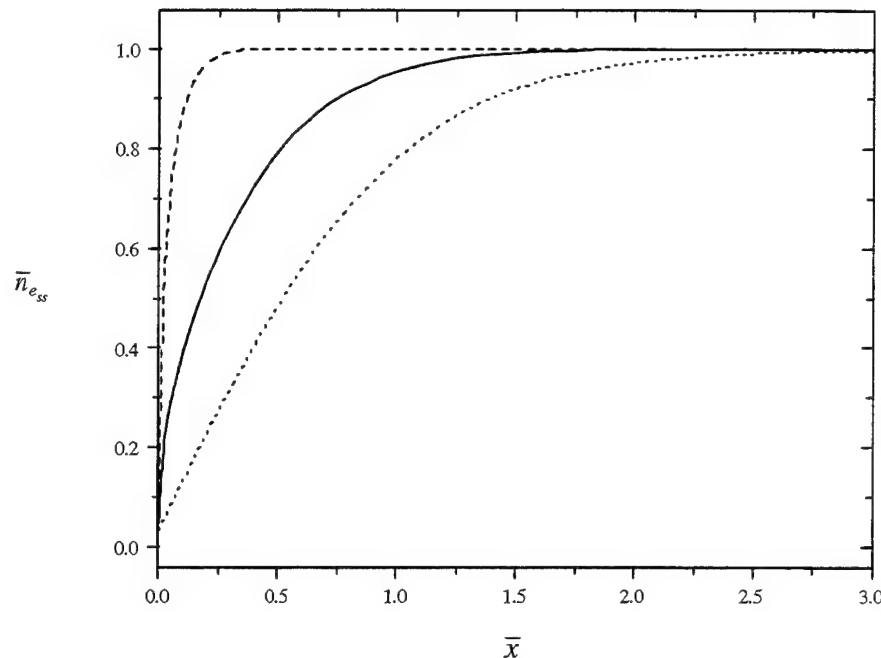
Figure 3.1. Profiles of the non-dimensional electron number density for $\overline{J} = 400$ (dashed), 40 (solid), and 0.4 (dotted). The curves are normalized by the farfield values, which are 4.51, 1.24, and 1.00 respectively.
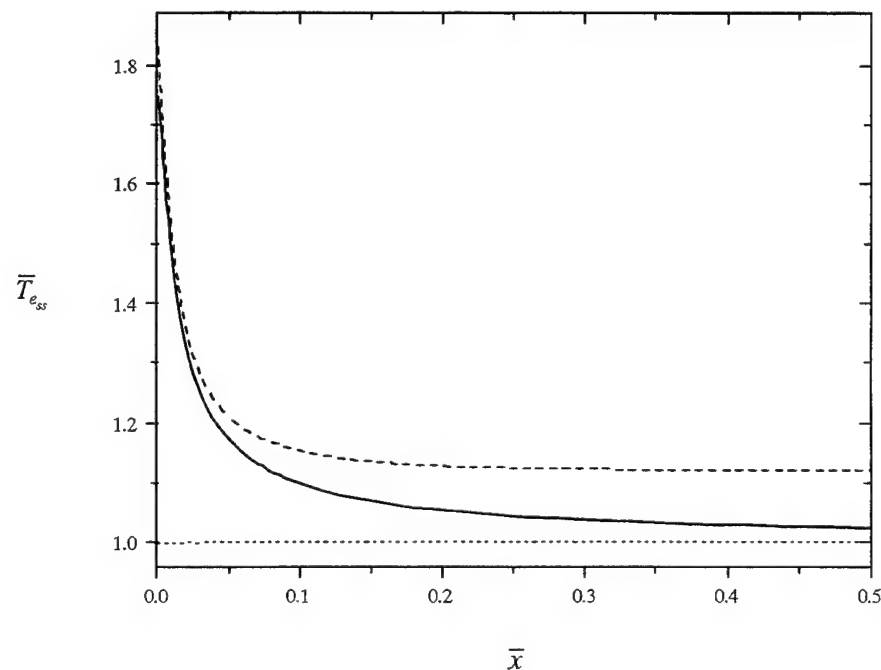

Figure 3.2. Profiles of the non-dimensional electron temperature for $\overline{J} = 400$ (dashed), 40 (solid), and 0.4 (dotted).

$\overline{E}_{ss}$

$\overline{x}$
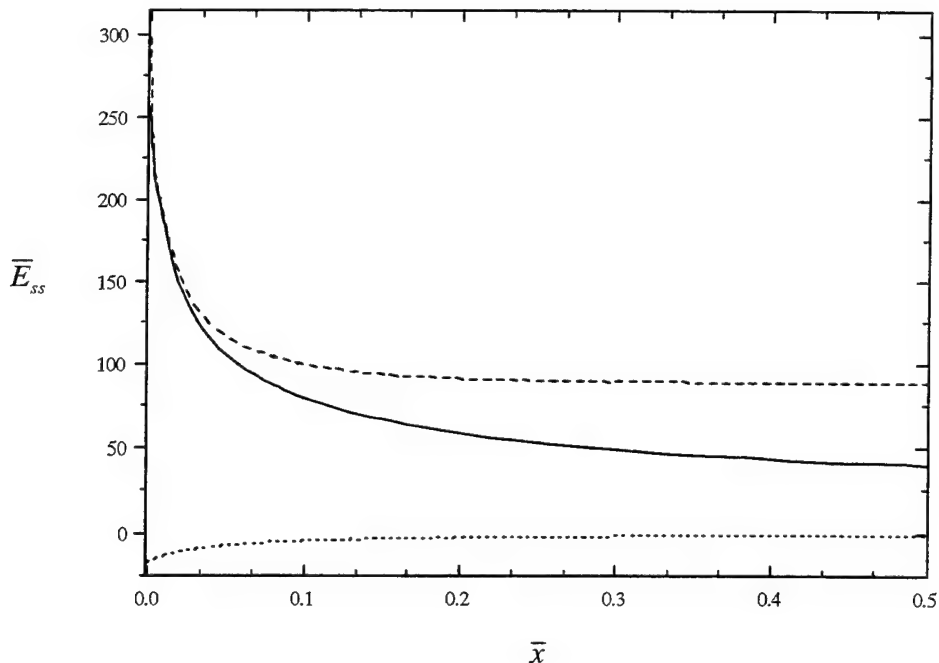
Figure 3.3. Profiles of the non-dimensional electric field for $\overline{J} = 400$ (dashed), 40 (solid), and 0.4 (dotted).

$\overline{n}_{ss}$

$\overline{x}$
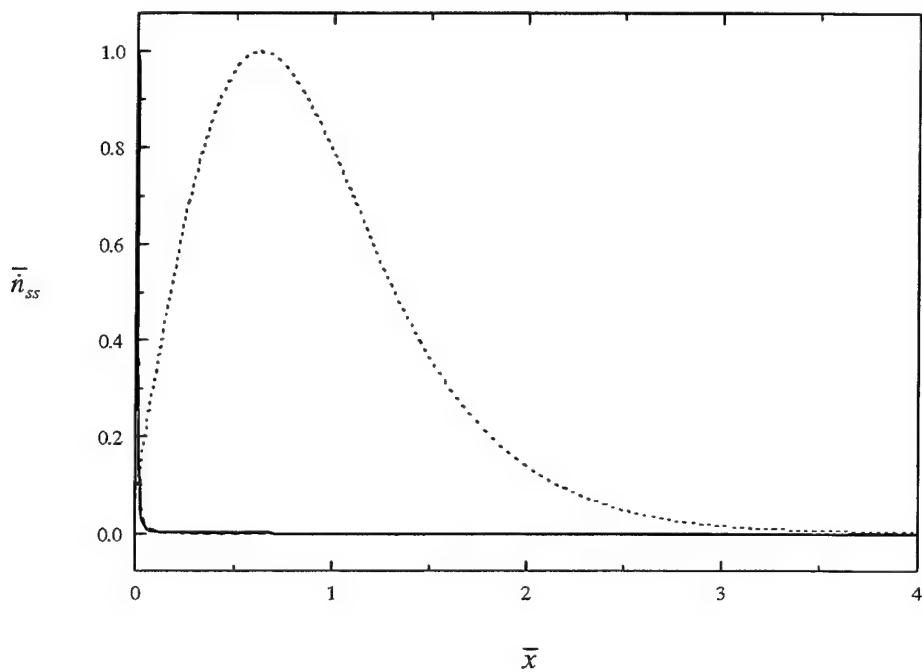
Figure 3.4. Profiles of the non-dimensional charged particle production rates for $\overline{J} = 400$ (dashed), 40 (solid), and 0.4 (dotted). The curves are normalized by their maximum values, which are $\overline{n}_{max} = 1.00 \times 10^4$, 863, and 0.385 respectively.
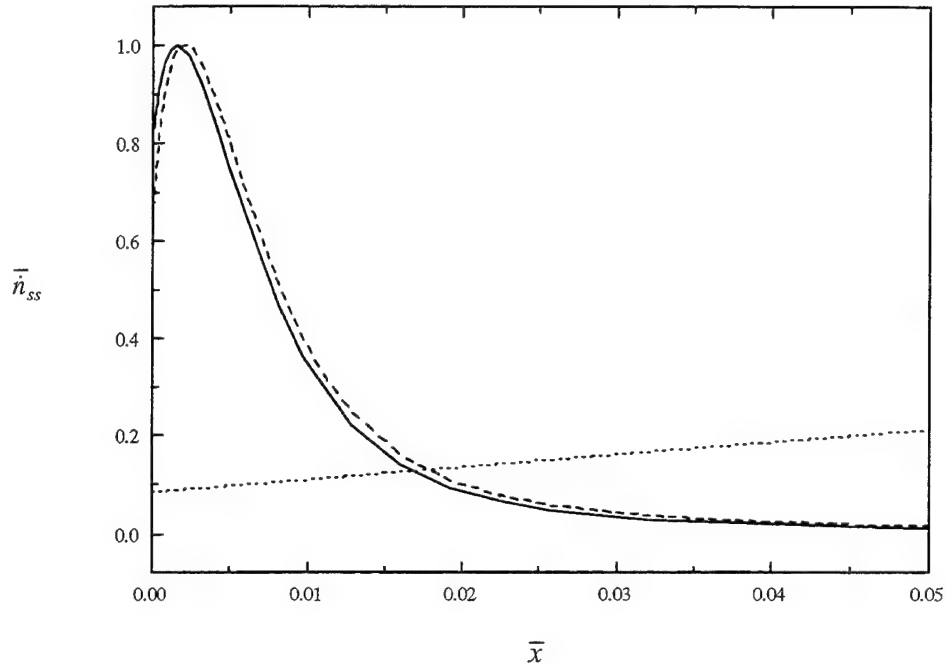
Figure 3.5. Near-anode view of Figure 3.4.
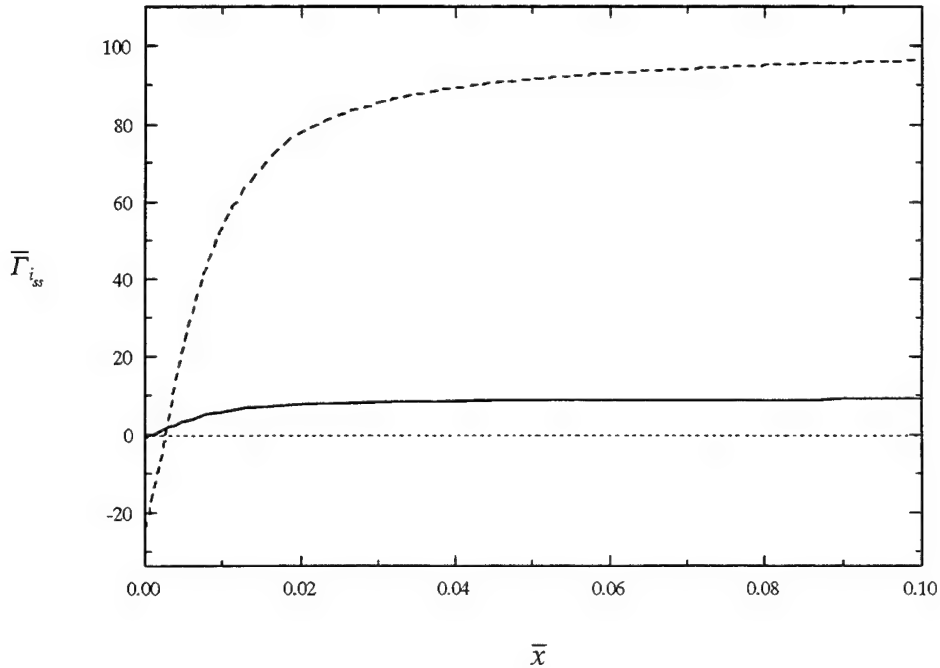
Figure 3.6. Profiles of the non-dimensional ion flux for $\bar{J} = 400$ (dashed), 40 (solid), and 0.4 (dotted).
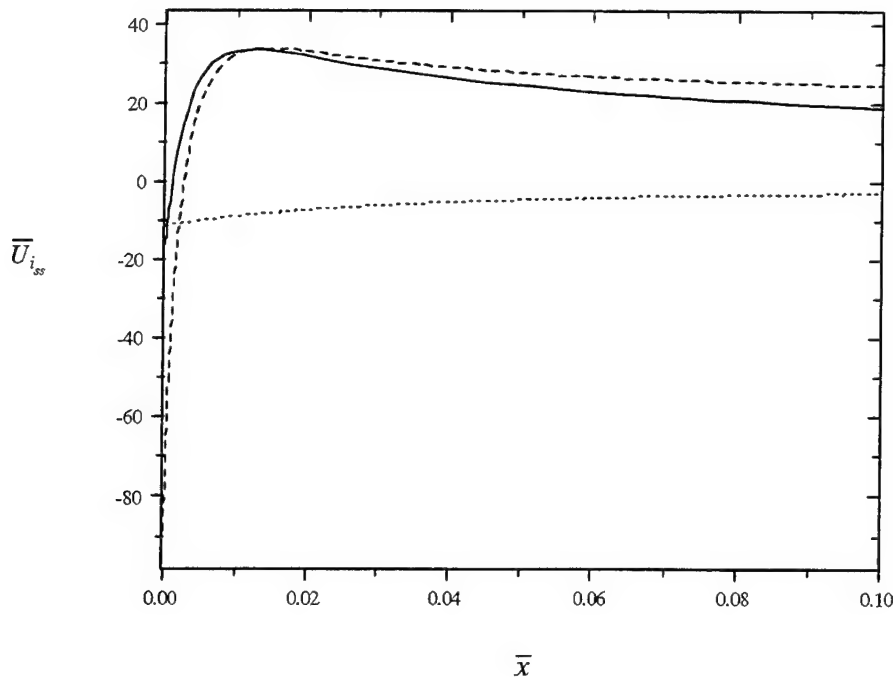
Figure 3.7.   Profiles of the non-dimensional ion velocity for $\overline{J} = 400$ (dashed), 40 (solid), and 0.4 (dotted).
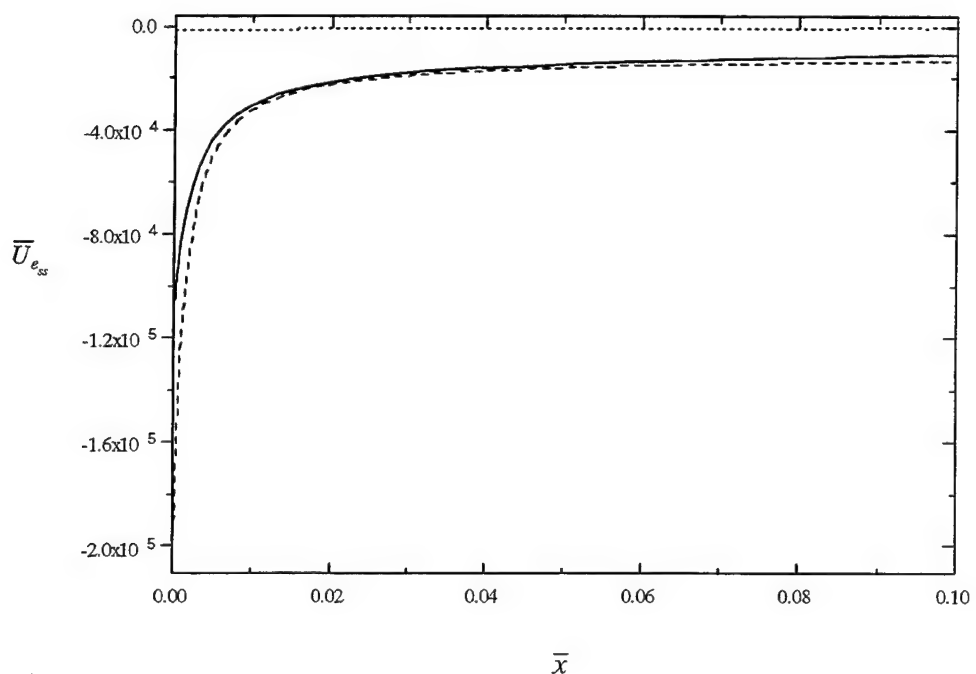

Figure 3.8. Profiles of the non-dimensional electron velocity for $\overline{J} = 400$ (dashed), 40 (solid), and 0.4 (dotted).

current density cases) as shown by Figs. 3.4 and 3.5, and as required by the three body recombination occurring at the anode.

For higher current densities, such as $\bar{J} = 40$ and 400, we see that the boundary layer exhibits additional characteristics. Most importantly, there exists a much stronger thermal non-equilibrium between the electrons and heavy particles. It is clear that for these particular cases there is significant heating of the electrons near the anode. This is due to the reduced conductivity caused by the loss of electrons and ions at the anode wall, which in turn forces the electric field to rise in order to maintain the required current density. The elevated electron temperatures contribute heavily to the increase in charged particle production for these higher current cases. As shown in Fig. 3.5, the region of ionization moves very close to the anode wall because of the combination of maximum electron temperatures and minimum charged particle number densities. This is in contrast to the $\bar{J} = 0.4$ case, where ionization is due to the depressed charged particle number densities alone.

3.4. The Assumption of Quasineutrality

As discussed in the previous chapter, the assumption of quasineutrality removes the ability to resolve the sheath in this model. Let us take a moment to comment on this issue. The equation we have left out is Poisson's equation:

$$\frac{dE}{dx} = \frac{n_i - n_e}{\varepsilon_0} \tag{3.4.1}$$

which, non-dimensionalized, appears as

$$\varepsilon^2 \frac{d\bar{E}}{d\bar{x}} = \bar{n}_i - \bar{n}_e \tag{3.4.2}$$

where $\varepsilon = \lambda_D / l_R$, the ratio of the debye length $\lambda_D = \sqrt{\varepsilon_0 k T_{e_R} / n_{e_R}^2}$ to the recombination scale length. When this equation is ignored, it is assumed that the electric field gradient is not great enough to warrant a significant difference between n_i and n_e. Another way to write this is

$$\varepsilon^2 \frac{d\overline{E}}{dx} \ll \overline{n}_e \qquad\qquad (3.4.3)$$

If this inequality is true, then the difference in n_i and n_e necessary to maintain the electric field gradient is very small compared to the actual value of n_e. For the conditions described in Table 3.1, we find that $\varepsilon = 4.6 \times 10^{-5}$. Plugging simple order of magnitude estimates for the field gradient shows that this condition is satisfied to a reasonable degree. Therefore, under these conditions, the assumption of quasineutrality is a reasonable simplification.

Chapter 4.

Stability Analysis - The Uniform Plasma Case

We begin the stability analysis by examining the simple situation of an initially uniform background plasma. With this simplification much can be learned about the effects of the physical mechanisms which are believed to cause or hinder instability without dealing with the additional complications associated with a spatially varying plasma.

4.1. Mathematical and physical preliminaries

The assumption of an initially uniform, unbounded plasma reduces the mathematical model to a homogeneous set of linear algebraic equations, rather than a set of homogeneous ordinary differential equations. Because of this uniformity, an additional simplification can be made with regard to the form of the perturbations described by eqn. 2.4.2. For this special case, we may assume that

$$\hat{\bar{f}}(\bar{x}) = \tilde{\bar{f}}e^{i\bar{k}\bar{x}} \tag{4.1.1}$$

where $\tilde{\bar{f}}$ is a constant and $\bar{k}$ is real-valued and denotes the non-dimensional wave number. The perturbation thus exhibits a pure sinusoidally varying spatial character. When combined with the oscillatory temporal behavior, the perturbation is interpreted as a traveling plane wave which can grow or decay in time. Even with these simplifications, the solution is still general because of the fact that an arbitrary 1-D perturbation can be decomposed into a sum of fourier components which have the traveling waveform of

$$\tilde{\bar{f}}e^{i\left(\bar{k}\bar{x}-\bar{\omega}t\right)}. \tag{4.1.2}$$

To analyze the problem for stability, we solve for the dispersion relationships of the waves, which involves solving a generalized eigenvalue problem to find the relationship between $\bar{\omega}$ and $\bar{k}$. For a specified wavenumber $\bar{k}$, we specifically search for conditions where the imaginary component of $\bar{\omega}$, $\bar{\omega}_i$, which is interpreted as the growth rate, is positive, indicating a *temporal* instability. The focus of this study will only be on temporal instabilities, as opposed to *spatial* instabilities, which involve the determination of the spatial growth rates $\mathrm{Im}(\bar{k})$ for a specified real frequency $\bar{\omega}$.

We suspect that the spatially non-uniform electrical boundary layer, which was shown in the previous chapter to be in a state of ionizational nonequilibrium, is more susceptible to instability than the far-field equilibrium plasma. To investigate the effect of ionizational non-equilibrium, we allow the uniform plasma to be underdense, meaning at an electron number density lower than that dictated by local thermodynamic equilibrium at the local electron number density and pressure. We therefore impose the existence of a constant ion/electron sink on the problem which, although unphysical, allows us to retain the simplicity of the uniform analysis while including many important physical mechanisms.

4.2. Steady behavior

We begin the analysis with the solution of the steady state equations which describe the background plasma. Because of the uniformity of the plasma, the equations reduce to simple algebraic relationships for ion velocity, electron velocity, electric field, and electron temperature. Although we ignore the steady ion and electron continuity equations and hypothetically model the presence of a charged particle sink and neutral particle source, we do take into account the production of charged particles due to perturbations in electron number density and temperature by including charged particle conservation in the set of disturbance equations.

Without the steady state continuity equations, we are left with the electron number density, in addition to the current density, as a free parameter. We are therefore free to choose the value of the electron number density and hence artificially set the initial steady state rate of ionization. The steady state, uniform equations used are merely eqns 2.3.3 - 2.3.6 (minus continuity) without the unsteady and gradient terms:

$$\overline{U}_e = -\frac{\overline{J}(1+\mu)}{4\overline{n}_e\mu} \tag{4.2.3}$$

$$\overline{U}_i = \frac{\overline{J}(1+\mu)}{4\overline{n}_e} \tag{4.2.4}$$

$$\overline{E} = \frac{\overline{J}}{\overline{n}_e} \tag{4.2.5}$$

$$\overline{U}_{e_{ss}}\overline{E} = -\frac{(1+\mu)}{4\mu}\left(\frac{\overline{J}}{\overline{n}_{e_{ss}}}\right)^2 = -3\theta\left(\overline{T}_{e_{ss}} - 1\right) - \overline{\varepsilon}_I\left[\overline{T}_{e_{ss}}^{-3}\ exp\left(\overline{\varepsilon}_I\left(1-\frac{1}{\overline{T}_{e_{ss}}}\right)\right) - \frac{\overline{n}_{e_{ss}}^2}{\overline{T}_{e_{ss}}^{\frac{9}{2}}}\right] \tag{4.2.6}$$

Figs. 4.1 and 4.2 give the variation in these computed steady state plasma properties as a function of the non-dimensional electron number density for a specified non-dimensional current of $\overline{J}$ = 363 (J = 1×10^5 A/m^2). The remaining properties are identical to those listed in Table 3.1.

It is apparent from Figs. 4.1 and 4.2 that as the electron number density (and hence conductivity) decreases, the electron temperature, electron and ion speed, and electric field increase.

4.3. Perturbation equations

With the simplifications provided by the assumption of an initially uniform plasma, the general perturbation equations, eqns. 2.4.3 - 2.4.7, are reduced to the following set of linear algebraic equations:
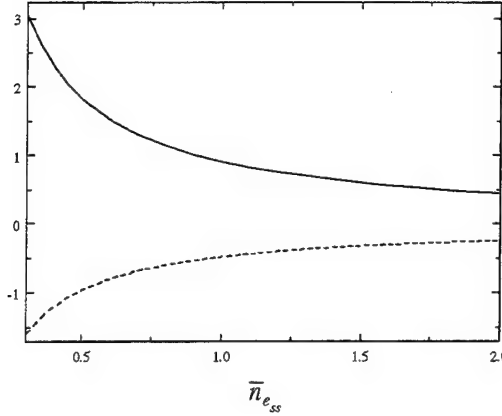
Figure 4.1. The steady, non-dimensional electron (dashed) and ion (solid) velocities vs. the electron number density. The curves are normalized by 10^5 and 100, respectively.
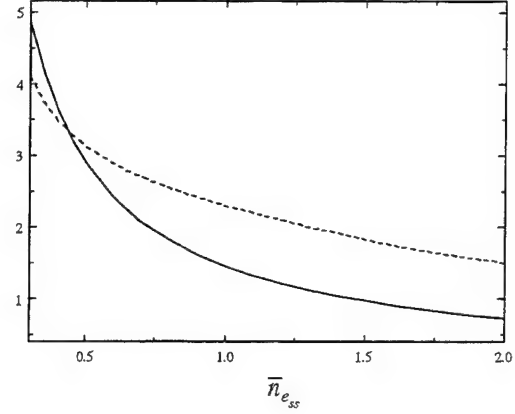
Figure 4.2. The steady, non-dimensional electric field (solid, normalized by 250) and electron temperature (dashed) vs. the electron number density.

$$-i\overline{\omega}\hat{\overline{n}}_e + i\overline{k}\left(\overline{U}_{e_{ss}}\hat{\overline{n}}_e + \overline{n}_{e_{ss}}\hat{\overline{U}}_e\right) =$$

$$\overline{T}_{e_{ss}}^{-3} \exp\left(\overline{\varepsilon}_I\left(1-\frac{1}{\overline{T}_{e_{ss}}}\right)\right)\left[\hat{\overline{n}}_e + \frac{\overline{n}_{e_{ss}}}{\overline{T}_{e_{ss}}}\left(\frac{\overline{\varepsilon}_I}{\overline{T}_{e_{ss}}}-3\right)\hat{\overline{T}}_e\right] + \frac{\overline{n}_{e_{ss}}^2}{\overline{T}_{e_{ss}}^{\frac{9}{2}}}\left[\frac{9}{2}\frac{\overline{n}_{e_{ss}}}{\overline{T}_{e_{ss}}}\hat{\overline{T}}_e - 3\hat{\overline{n}}_e\right] \qquad (4.3.1)$$

$$\left(\overline{U}_{e_{ss}} - \overline{U}_{i_{ss}}\right)\hat{\overline{n}}_e + \overline{n}_{e_{ss}}\left(\hat{\overline{U}}_e - \hat{\overline{U}}_i\right) = 0 \qquad (4.3.2)$$

$$-i\overline{\omega}\frac{4}{(1+\mu)\nu_{in}t_R}\frac{m_e}{m_i}\overline{n}_e\hat{\overline{U}}_e = -\overline{n}_{e_{ss}}\hat{\overline{E}} - \overline{E}_{ss}\hat{\overline{n}}_e - i\overline{k}\overline{n}_{e_{ss}}\hat{\overline{T}}_e - i\overline{k}\overline{T}_{e_{ss}}\hat{\overline{n}}_e - \frac{4\mu}{1+\mu}\left(\overline{n}_{e_{ss}}\hat{\overline{U}}_e + \overline{U}_{e_{ss}}\hat{\overline{n}}_e\right)$$

$$(4.3.3)$$

$$-i\overline{\omega}\frac{4}{(1+\mu)\nu_{in}t_R}\overline{n}_e\hat{\overline{U}}_i = \overline{n}_{e_{ss}}\hat{\overline{E}} + \overline{E}_{ss}\hat{\overline{n}}_e - i\overline{k}\hat{\overline{n}}_e - \frac{4}{1+\mu}\left(\overline{n}_{e_{ss}}\hat{\overline{U}}_i + \overline{U}_{i_{ss}}\hat{\overline{n}}_e\right) \qquad (4.3.4)$$

$$-\frac{3}{2}i\overline{\omega}\hat{\overline{T}}_e + \frac{3}{2}i\overline{k}\overline{U}_{e_{ss}}\hat{\overline{T}}_e + i\overline{k}\overline{T}_{e_{ss}}\hat{\overline{U}}_e - \frac{8\mu}{1+\mu}\overline{U}_{e_{ss}}\hat{\overline{U}}_e$$

$$= 3\theta\hat{\overline{T}}_{e_e} - \frac{3}{5}\left(\frac{1+\mu}{\mu}\right)\overline{k}^2\overline{T}_{e_{ss}}\hat{\overline{T}}_e - \overline{\varepsilon}_I\overline{T}_{e_{ss}}^{-4}\exp\left(\overline{\varepsilon}_I\left(1-\frac{1}{\overline{T}_{e_{ss}}}\right)\right)\left(\frac{\overline{\varepsilon}_I}{\overline{T}_{e_{ss}}}-3\right)\hat{\overline{T}}_e - \frac{9}{2}\overline{\varepsilon}_I\frac{\overline{n}_{e_{ss}}^2}{\overline{T}_{e_{ss}}^{\frac{11}{2}}}\hat{\overline{T}}_e + \frac{2\overline{\varepsilon}_I\overline{n}_{e_{ss}}}{\overline{T}_{e_{ss}}^{\frac{9}{2}}}\hat{\overline{n}}_e \ .$$

$$(4.3.5)$$

These equations represent a balance of stabilizing (damping) terms, destabilizing (growth) terms, and terms whose effect on stability is not obvious by inspection. The first two types of terms are those for which the perturbed property (electron number density, temperature, etc) is the same as that of the unsteady term (the term which contains ω). For example, consider the following linear ordinary differential equation:

$$\frac{dy}{dt} = \pm ay \qquad (4.3.6)$$

The solution to this o.d.e has the form

$$y = e^{\pm at} + c \qquad (4.3.7)$$

which denotes either an exponentially decaying (-) or growing (+) temporal solution. If we substitute the operator $d/dt = -i\omega$, we obtain

$$-i\omega y = \pm ay \qquad (4.3.8)$$

which is a form present in each of the perturbation equations. Hence, we can see that in the electron continuity equation, the group

$$\left(\overline{T}_{e_{ss}}^{-3} \, exp\left(\overline{\varepsilon}_I\left(1 - \frac{1}{\overline{T}_{e_{ss}}} \right) \right) - 3\frac{\overline{n}_{e_{ss}}^2}{\overline{T}_{e_{ss}}^{\frac{9}{2}}} \right) \hat{\overline{n}}_e \qquad (4.3.9)$$

contains both a growth and a damping term.

Terms which contain the same perturbed property as the unsteady term but additionally are multiplied by $\pm i$ can also be classified. The main effect of these terms is on the frequency of oscillation, and are hence hereafter referred to as "frequency" terms. This can be clarified by considering the real and imaginary parts of, for example, the

electron continuity perturbation equation separately, and examining how the real and imaginary parts of ω are affected by the terms in the equation (multiplication by i can also be thought of as a 90 degree shift in relative phase). For example, consider the first two terms

$$-i\overline{\omega}\hat{n}_e + i\overline{k}\overline{U}_{e_{ss}}\hat{n}_e + \dots \tag{4.3.10}$$

of the continuity perturbation equation. It is clear in this example that the second term affects only the real component of ω, the frequency of oscillation, and is hence a "frequency" term.

The remaining terms which cannot be classified in any of these ways have in general a combined effect on the stability and dispersion characteristics of the perturbations. The prime factors for determining the effect of these terms on the disturbances, whether stabilizing or destabilizing, are the relative phase and amplitude of the perturbations.

Another thing to note is that in the momentum equations, the coefficient of the unsteady terms ($4/\left((1+\mu)v_{in}t_R\right)$ for ion momentum equation) are very small, signifying that the unsteady terms are negligible for frequencies much smaller than the ion-neutral collision frequency. Therefore, the unsteady terms in the momentum equations can be ignored for most frequencies of interest; the momentum equations would then describe a balance between the pressure, field, and collisional forces due to the perturbations. This also implies that for these frequencies, the stability and dispersion characteristics are mainly determined by the continuity and electron energy equations.

4.4. The Role of Ionization

Examination of eqn. 4.2.6, the steady state electron energy equation, reveals that it is non-linear in $\overline{T}_e$ and therefore must be solved for a given electron number density and current density by using an iterative technique. Ignoring for now the recombination term (the last term within the brackets), we have an expression for the rate of energy dissipation for the given current and electron number density. Plotting the right hand side with respect to $\overline{T}_e$, as shown in Fig. 4.3, reveals a maximum value of energy that can be dissipated by collisions and ionization, which approximately corresponds to the maximum rate of charged particle production. This maximum occurs at the condition:

$$\overline{T}_e = \frac{\overline{\varepsilon}_I}{3} \tag{4.4.1}$$
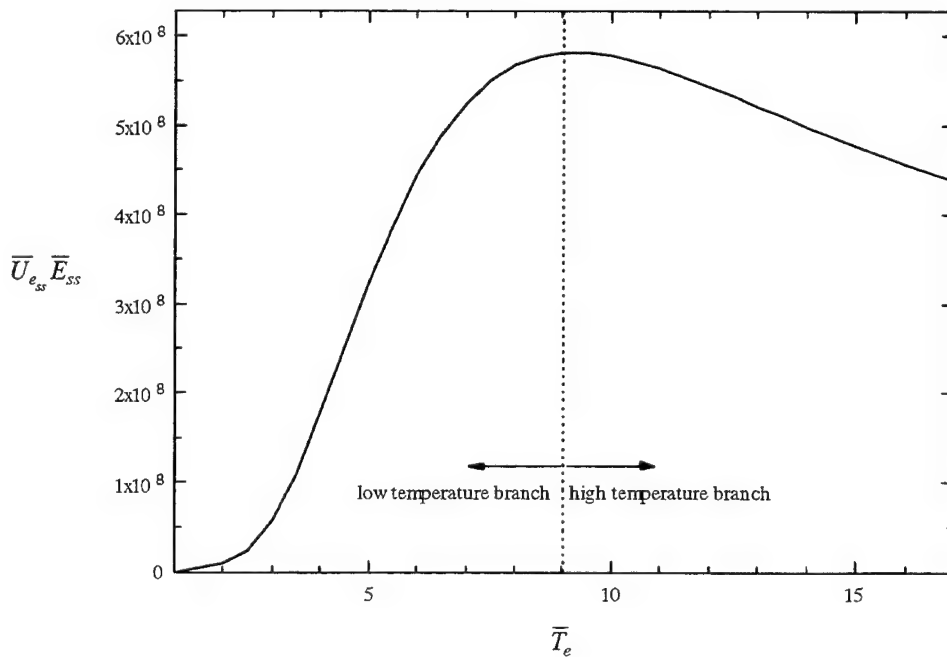
Figure 4.3. Variation in rate of energy loss due to ionization and collisional energy exchange with electron temperature.

or, dimensionally,

$$T_e = \frac{\varepsilon_I}{3k}.$$ (4.4.2)

For atomic hydrogen this corresponds to a value of 52609 K, or 4.53 ev.

With Fig. 4.3 we may begin to speculate on the mechanisms and conditions which might cause small perturbations to become unstable. On the high temperature branch (temperatures greater than that corresponding to the maximum point), a small increase in (electron) temperature, by way of a perturbation, results in a decrease in the rate of energy dissipation. If that temperature perturbation is accompanied by a positive perturbation to the energy addition rate (from the joule heating and pressure work mechanisms), then the result may be an initial runaway increase in the temperature. A runaway situation can also happen if the opposite process occurs, i.e if on the low temperature branch, a decrease in the electron temperature leads to an increase in energy addition. Another possibility is that an increase in temperature causes an increase in energy dissipation which is smaller than the increase in energy addition. The slope of the curve determines this increase in energy dissipation, which implies that regions of the curve with shallower slopes would tend to be more susceptible to instability. Thus, although the point of inflection may seem like an obvious place for instability to occur, the actual location of the demarcation between temporally stable and unstable situations is unclear and must be determined using an unsteady analysis. Note that this simple thought experiment does not take into account mechanisms such as conduction and pressure work which also have an effect on stability.

The ionization rate perturbation is given in the right hand side of the electron continuity equation. We dimensionalize this term by multiplying it with $\dot{n}_R$, the reference production rate. The resulting dimensional production rate, $\dot{n}_e$, is written as

$$\beta\left(T_{e_R}\right)\overline{n}_{e_R}^2 \ exp\left(\overline{\varepsilon}_I\left(1-\frac{1}{\overline{T}_{e_{ss}}}\right)\right)\left(\hat{n}_e - \frac{\overline{n}_{e_{ss}}}{\overline{T}_{e_{ss}}}\left(\frac{\varepsilon_I}{kT_e}-3\right)\hat{T}_e\right)$$

(4.4.3)

The coefficient of this term,

$$\beta\left(T_{e_R}\right)\overline{n}_{e_R}^2 \ exp\left(\overline{\varepsilon}_I\left(1-\frac{1}{\overline{T}_{e_{ss}}}\right)\right),$$

(4.4.4)

which we will denote the "production coefficient," provides a reasonably simple way of quantifying the increase in charged particle production due to perturbations in electron number density and temperature. For higher values of this coefficient, more charged particles are produced for a given perturbation in electron number density and temperature, which could result in a stronger instability. Care must be taken in this interpretation, however, because it does not take into account changes in relative phase of the electron number density and temperature perturbation resulting from changes in $\overline{k}$. Also, when comparing the stability of different steady state conditions, it must be noted that the terms involving the perturbations in equations 4.3.1 - 4.3.5 also depend on the steady state conditions.

4.5. Solution

Eqns. 4.3.1 - 4.3.5 can be expressed as a generalized eigenvalue problem, with $\overline{\omega}$ as the eigenvalue. The form of this eigenvalue problem is

$$\left[\vec{\vec{A}} - \omega\vec{\vec{B}}\right]\vec{y} = 0$$

(4.5.1)

where

$$\vec{y} = \begin{bmatrix} \hat{\bar{n}}_e & \hat{\bar{U}}_e & \hat{\bar{U}}_i & \hat{\bar{E}} & \hat{\bar{T}}_e \end{bmatrix}^T, \text{ the perturbation amplitudes}$$

and

$\left[\vec{\vec{A}} - \bar{\omega}\vec{\vec{B}} \right]$ is the coefficient matrix of the perturbation eqns. 4.3.1 - 4.3.5.

The solution of such a problem can be handled by using a standard routine found in many commercial matrix analysis programs such as *Matlab*. However, it is also informative to consider an analytical method:

$$det\left[\vec{\vec{A}} - \bar{\omega}\vec{\vec{B}} \right]\vec{y} = 0 \tag{4.5.2}$$

This statement can then be reduced to an algebraic equation using a symbolic math program such as *Mathematica*. The resulting equation is a third order polynomial, which denotes that three "eigenmodes" are possible for each steady state condition. Each eigenmode has a distinct value for $\bar{\omega}$, the complex eigenvalue, as well as its own set of perturbation amplitudes.

4.6. Isothermal waves

The solution of the perturbation equations for temporal stability reveals that there are three modes which can propagate and grow (or decay) in this initially uniform plasma. As a matter of convenience we wish to identify these modes and assign a nomenclature to them so that they can be identified for different steady state conditions. To facilitate this, we study a simplified "isothermal" model which gives an analytical solution for the eigenvalues. We form the isothermal model from the set of perturbation equations by fixing the electron temperature at the temperature of the heavy particles, thus removing the need for the electron energy equation. Setting the determinant of the resulting system to zero, we obtain the following quadratic equation for ω:

$$\overline{\omega}^2 - \overline{k}\,\overline{\omega}\left(\frac{m\overline{U}_{e_{ss}} + \overline{U}_{i_{ss}}}{1+m}\right) - i\overline{\omega}\left(1 - 3\overline{n}_{e_{ss}}^2 - v_{in}t_R\frac{1+\mu}{1+m}\right) + v_{in}t_R\frac{1+\mu}{1+m}\left(1 - 3\overline{n}_{e_{ss}}^2\right) - \frac{\overline{k}^2}{2}\frac{1+\mu}{1+m}v_{in}t_R = 0$$

$$(4.6.1)$$

where $m = m_e/m_i$. From this equation, we find that one root has the approximate value:

$$\overline{\omega} \approx \overline{k}\,\overline{U}_{i_{ss}} - iv_{in}t_R \qquad (4.6.2)$$

which we identify as an "ion" disturbatnce, since the phase velocity of the wave ($\overline{\omega}_R/\overline{k}$) is very close to the ion velocity. We shall see in next section that this mode is characterized by a comparitively large ion velocity disturbance, hence additionally justifying its nomenclature.

We refer to the other mode as the "pressure" disturbance, because it is found to be more closely driven by gradients in the electron number density and electron temperature. Setting the inelastic energy loss factor, δ_h, to a very high value and solving the full set of perturbation equations also reveals these two isothermal modes. In essence δ_h affects the degree of departure of the electrons from thermal equilibrium. When the non-isothermal case is investigated ($\delta_h = 5$, a typical value for hydrogen) as described below, a third mode appears, which we associate with the electron energy equation and thus identify as a "thermal" wave. This assignment is also related to the fact that this third mode has a damping rate that is characterized by the energy dissipation coefficients

$$\overline{\varepsilon}_I\frac{exp\left(\overline{\varepsilon}_I\left(1-\frac{1}{\overline{T}_{e_{ss}}}\right)\right)}{\overline{T}_{e_{ss}}^4}\left(\frac{\overline{\varepsilon}_I}{\overline{T}_{e_{ss}}} - 3\right) + 3\theta \qquad (4.6.3)$$

in the electron energy perturbation equation.

4.7. Results

4.7.1 Wave Characteristics

We now examine the dispersion characteristics of the three wave modes identified from the analysis. Of these three modes, the thermal wave is the most significant because it is the only one which exhibits unstable behavior. This illustrates the point that not every oscillatory perturbation behaves in the same way with regards to stability, reinforcing the notion that an unsteady analysis must be used to determine stability characteristics. In electrothermal instability theory, a positive perturbation in temperature is automatically assumed to result in a positive perturbation in charged particle number density. However, we shall see that this is not generally true and that many time scale and spatial factors contribute to the stability characteristics we are interested in.

In this section the dispersion characteristics of the three wave modes for a plasma at 6000 K drawing a non-dimensional current density of $\bar{J} = 400$ are presented. This current density is typical of the near anode current densities calculated in low power arcjet thrusters. The remaining parameters are again given in Table 3.1. A set of calculations is made with $\bar{n}_e = 0.5$ and $\bar{T}_e = 3.13$, which dimensionally correspond to ~ 8×10^{18} m^{-3} and 18,000 K. Most information that is needed to discuss the behavior of the three modes can be seen in the plots of the dispersion characteristics, growth/decay rates, and relative phase and amplitude vs. wave number, which are presented in Figs. 4-13.

We begin our discussion with the analysis of the ion wave mode, whose dispersion and growth/damping rate curves are given in Figs. 4.4 and 4.5, respectively. By examining its growth rate, we see that it remains fairly constant at a value of about 3×10^8, which, when dimensionalized (divided by t_R) gives 8.4×10^9 s^{-1}, the ion-neutral collision frequency. Fig. 4.6, which shows the ion velocity amplitude normalized by the electron velocity amplitude, shows that the ion velocity perturbation amplitude is very
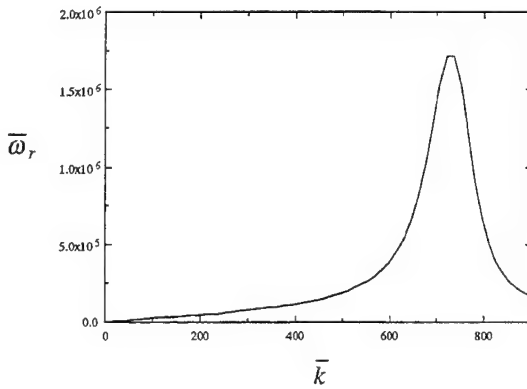
Figure 4.4. Dispersion curve for the ion mode.
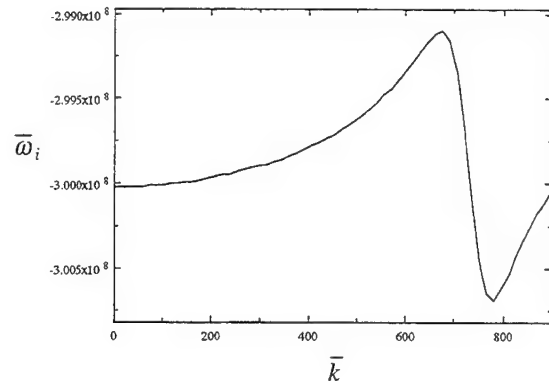
Figure 4.5. Growth rate curve for the ion mode.
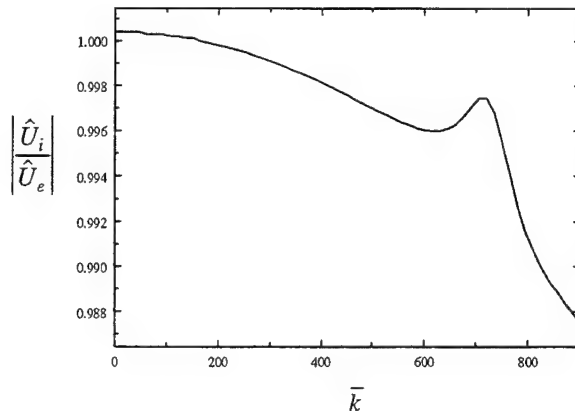
Figure 4.6. Ion/Electron velocity amplitude for the ion mode.

nearly equal to the electron velocity perturbation amplitude. This is not the case with the other two wave modes, in which the electron velocity perturbation amplitude is much larger than that of the ions. These two observations help confirm the fact that the "ion" wave is a disturbance that is in fact dominated by ion motion. Because of this, the dominant equation for this mode is the ion momentum equation, which, upon removal of field and pressure force terms (since they are small), becomes a equation relating the unsteady (inertia) term to the collisional damping term,

$$-i\omega \frac{4}{(1+\mu)\nu_{in}t_R}\bar{n}_e\hat{\bar{U}}_i \approx -\frac{4}{1+\mu}\bar{n}_{e_{ss}}\hat{\bar{U}}_i \Rightarrow \bar{\omega} \approx \nu_{in}t_R \qquad (4.7.1)$$

which explains the damping rate and behavior of this mode.

The thermal and pressure modes, in contrast, are modes where the ion velocity perturbation amplitude is much smaller than that of the electron velocity. Thus, the electron number density, temperature, and velocity perturbations are the dominant properties in these modes. Of the two modes, the thermal wave is of greater interest because of its potential for instability. Figs. 4.7 - 4.10 show the dispersion and growth/decay characteristics for these modes. An interesting point on these graphs is the $\bar{k} = 0$ point. At this infinite wavelength condition, many of the terms in the perturbation equations drop out, leaving only certain growth/damping (such as the energy dissipation and Joule heating) terms to balance the unsteady terms. In addition, these growth/decay terms remain constant for all values of $\bar{k}$, signifying that any changes in character for non-zero values of $\bar{k}$ are due to the remaining terms, which include the mechanisms of ion/electron flux, pressure force, energy convection, pressure work, and electron energy conduction.

From Figs. 4.7 - 4.10, we see that at $\bar{k} = 0$, the frequency of oscillation ω_r is zero and ω_i is negative, indicating a perturbation which decays uniformly. Therefore, without the influence of the "gradient" type mechanisms, the uniform underdense plasma is still stable. However, as seen from Fig. 10, for certain values of $\bar{k}$, the perturbation is unstable. The instability is hence dependent on these mechanisms for instability, indicating that the Joule heating perturbation alone is not sufficient for instability in these conditions.

The behavior of the thermal wave's stability characteristics can be partially clarified by examining figure 11, a plot of the relative phase between the electron number density and temperature perturbation. For the thermal wave, we see that the relative phase starts at 180 degrees for $\bar{k} = 0$. Eqn. 2.4.3 (the continuity pert equation) shows that the term
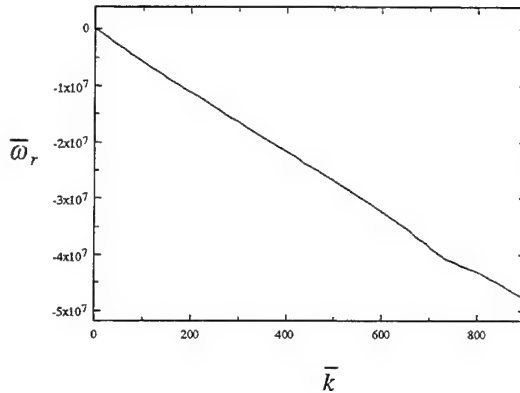
Figure 4.7. Dispersion curve for the pressure
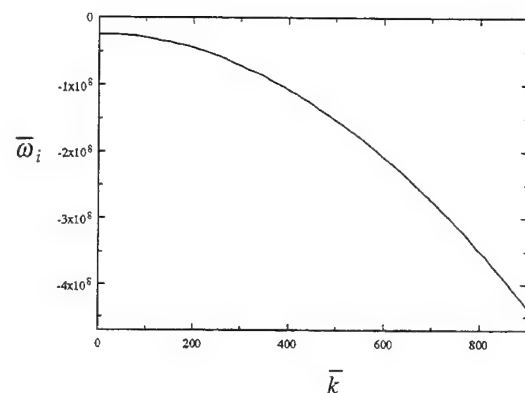
Figure 4.8. Growth rate curve for the pressure
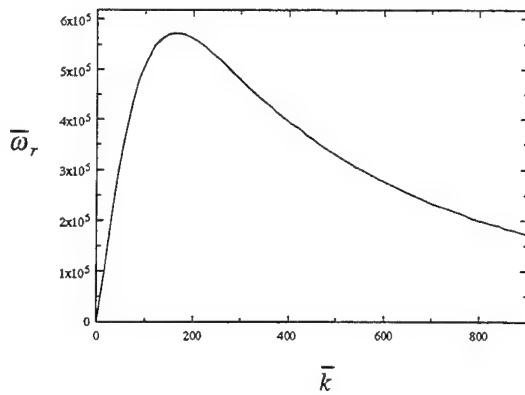
Figure 4.9. Dispersion curve for the thermal
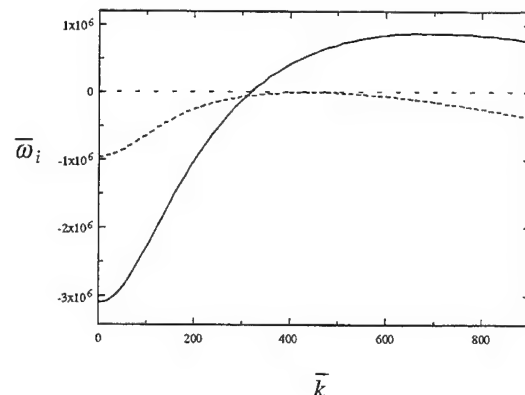
Figure 4.10. Dispersion curve for the thermal mode. The dashed line denotes a "critical" condition where $\overline{n}_{e_{ss}} = 0.9$.

$$\overline{T}_{e_{ss}}^{-3} \, exp\left(\overline{\varepsilon}_I\left(1 - \frac{1}{\overline{T}_{e_{ss}}} \right) \right)\hat{\overline{n}}_e \tag{4.7.2}$$

is a growth term. The perturbation to charged particle production due to the electron temperature perturbation is

$$\overline{T}_{e_{ss}}^{-3} \, exp\left(\overline{\varepsilon}_I\left(1 - \frac{1}{\overline{T}_{e_{ss}}} \right) \right)\left[\frac{\overline{n}_{e_{ss}}}{\overline{T}_{e_{ss}}}\left(\frac{\overline{\varepsilon}_I}{\overline{T}_{e_{ss}}} - 3 \right)\hat{\overline{T}}_e \right], \tag{4.7.3}$$
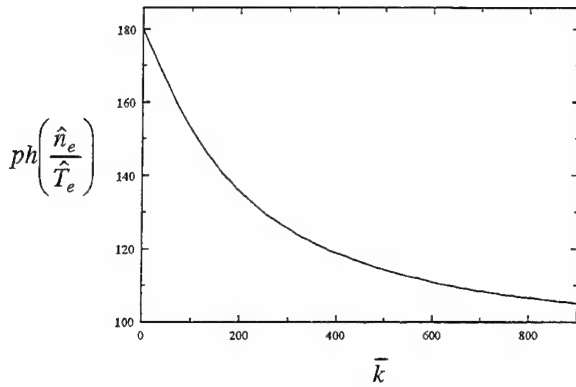
Figure 4.11. Relative phase between
the electron number density and
temperature for the thermal mode.
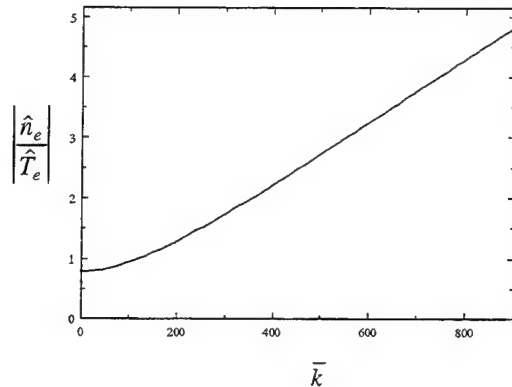
Figure 4.12. Relative amplitude
between the electron number density
and temperature for the thermal mode.
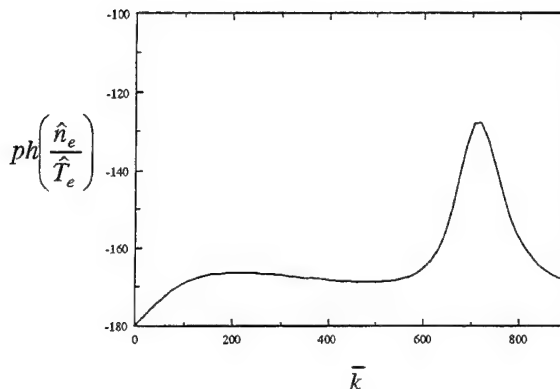
Figure 4.13. Relative phase between
the electron number density and
temperature for the pressure mode.
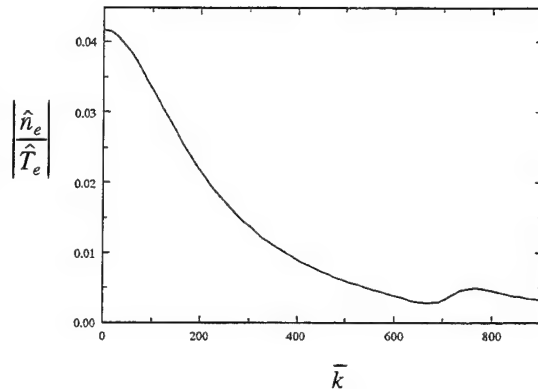
Figure 4.14. Relative amplitude
between the electron number density
and temperature for the pressure mode.

which will be a pure damping term if the relative phase is 180 degrees, and a pure growth term if the it is 0 degrees.   At 90 or 270 degrees the temperature perturbation has no effect on the growth or decay of the electron number density;   its main effect is on the frequency of oscillation.   This can again all be seen by considering the real and imaginary parts of the electron continuity equation separately, and examining how the real and imaginary parts of ω are affected by the different terms in the equation.   As $\overline{k}$ increases, the relative phase decreases, signifying that the opposing effect of the two perturbations on the production perturbation is reduced at higher wave numbers. Therefore the growth of the electron number density is due to the increase of charged particles caused by the perturbation in the electron number density.   We thus conclude

that in this mode the temperature perturbation does not contribute to the overall increase in charged particle production.

The relative amplitude of the number density perturbation compared to the temperature perturbation also increases with $\bar{k}$, as shown in Fig. 4.12. Again, this helps explain why the thermal mode becomes unstable at certain $\bar{k}$.

The growth rate shows a maximum value at $\bar{k} \sim 700$. This maximum exists because of the influence of electron energy conduction, which is clearly a damping mechanism with a quadratic dependence on the wavenumber. Hence, at high wavenumbers, the conduction term becomes an increasingly important stabilizing mechanism.

The same phase and amplitude plots are given for the pressure mode in Figs. 4.13 and 4.14. For this mode we see that the relative phase between the number density and temperature remains for the most part fairly close to 180 degrees with changing $\bar{k}$, with the number density amplitude also dropping with respect to the temperature amplitude. This behavior, which is contrary to that of the thermal wave, helps explain why the decay rate grows with $\bar{k}$, and why the mode never becomes unstable.

A very interesting thing to point out is that if the pressure work, convection, and conduction terms in the electron energy perturbation equation are removed, the critical electron temperature increases to 8.1 ev, which corresponds to a dimensional electron temperature of almost 50,000 K. In this temperature regime Joule heating is very high and the slope of the curve in Fig. 4.3 is small. This signifies that Joule heating alone is not a dominant mechanism in the instability at lower electron energies. Because the convection term acts as a "frequency" term, the main contributer, either directly or indirectly, to instability must be the pressure work perturbation, where its main influence may be its effect on the phase relationships between the perturbed quantities. It should

be remembered that the pressure work term does not destabilize the pressure or ion modes, implying that it can also act as a damping mechanism in these modes.

4.7.2. Critical conditions

We define the maximum value of $\bar{n}_{e_{ss}}$ (and hence minimum $\bar{T}_{e_{ss}}$) where the curve of $\bar{\omega}_i$ for the thermal mode just becomes positive at any value of $\bar{k}$ as the "critical" value of $\bar{n}_{e_{ss}}$. Fig. 10 shows the growth/decay rate curves for two values of $\bar{n}_{e_{ss}}$: the original value of 0.5, and the critical value of 0.9. Here it can be seen that as the number density drops, the instability becomes stronger. In this section we discuss how the critical conditions are affected by varying properties of the background gas such as the ionization energy, pressure, and temperature.

Examination of the steady state equations 4.2.3 - 4.2.6 shows that, for conditions where recombination can be neglected, the electron velocity, ion velocity, electric field, and electron temperature are all functions of the parameter $\bar{J}/\bar{n}_{e_{ss}}$, $\bar{\varepsilon}_I$, θ, and μ. Under the conditions of a constant background temperature T_R, background pressure P, gas type, collision frequencies v_{in} and v_{en}, and inelastic energy loss factor δ_h, the last three parameters are constant. For this idealized condition the solution to the steady state equations are solely determined by the non-dimensional ratio of current density to electron number density, which is equal to the non-dimensional electric field. This is not quite true in the case of the perturbation equations due to the presence of $\bar{n}_{e_{ss}}$ by itself in the continuity and momentum equations. However, we have found that despite this fact, the critical $\bar{J}/\bar{n}_{e_{ss}}$ value is essentially constant and a good parameter to use in determining stability characteristics. Hence, within the limits of this simplified model, smaller current densities could exhibit instabilities at lower electron number densities because of the higher rates of ionization, while larger current densities can become unstable for smaller departures from Saha equilibrium. Fixing this non-dimensional

parameter also fixes the critical electron temperature, which can similarly be viewed as a stability criterion.

4.7.2.1. Ionization Energy

The ionization energy would seem to be an important parameter in determining the stability characteristics of a uniform underdense plasma because of its influence on charged particle production rates. To isolate the effect of the ionization energy on stability, stability calculations are made with varying values of ε_I for $T = 6000$ K, $J = 1.1 \times 10^5$ A/m^2. This is a simple way learn about the stability characteristics of different gases, though variations in degenerate states, inelastic collision factors, collision frequencies, etc. are ignored because they cloud the analysis with additional complications.

The effect of ionization energy on stability is not obvious from an inspection of the perturbation equations. This is because while lower ionization energies give rise to higher production rates for a given electron number density and temperature, the energy dissipated by each charged particle pair produced is lower. Hence, there are competing factors whose overall influence on the critical conditions is not clear. The critical conditions are calculated and presented in Figs. 4.15 and 4.16, which show $\overline{T}_{e_{crit}}$ and $\overline{n}_{e_{crit}}$ versus ε_I Here, simple relationships are seen between these parameters. Our cutoff is $\varepsilon_I = 8$ ev, below which the critical electron temperature drops below the background temperature, hence entering a regime where there is steady state collisional energy *gain*. The critical electron temperature seems to vary linearly with ε_I, with higher ionization energies corresponding to higher values of $\overline{T}_{e_{crit}}$. The critical electron number density correspondingly falls with increasing ionization energy. The size of variation is not large, differing by roughly a factor of 2 between ionization energies ranging from 8 to 16. Because of this, the ratio $\overline{J}/\overline{n}_{e_{ss}}$, which describes the critical steady state electric field,
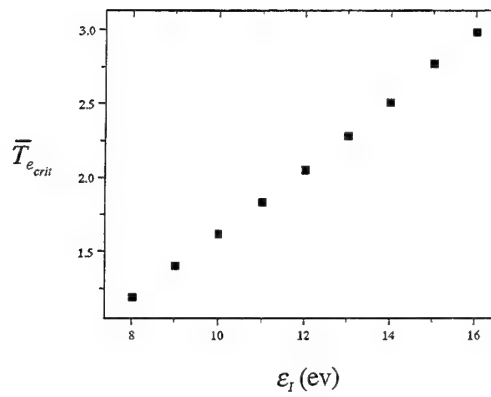
Figure 4.15. Critical non-dimensional
electron temperature vs. Ionization
energy.
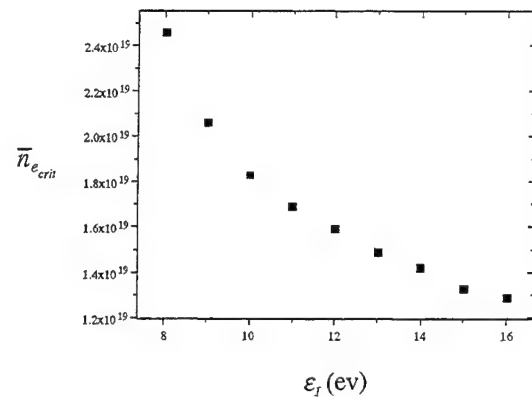
Figure 4.16. Critical non-dimensional
electron number density vs. Ionization
energy.

increases with ionization, implying that gases with higher ionization energies tend to be more stable.

We define the wavenumber for which the growth rate is zero as the critical wavenumber $\bar{k}_{crit}$. In performing the critical conditions analysis we find that the critical wavenumber stays on the order of 10^4 m^{-1} (with a tendency to decrease with increasing ionization energy), corresponding to a critical wavelength of 0.6 millimeters.

4.7.2.2. Pressure dependence (T = 6000, ε_I=13.6 ev)

The changes in stability characteristics due to varying background (neutral species) pressure is presented in this section. The influence of changing the background pressure is felt mainly on the charged particle production rate and the charged particle collision frequencies, both of which depend linearly on the neutral number density. The calculated critical conditions are presented in Table 4.1 for background pressures ranging from .1 atm to 10 atm. They show, interestingly, that the pressure has no effect on the critical electron temperature and number density, and that the main changes are in the growth/damping rates and critical wavenumbers. Increasing the background pressure while maintaining a fixed background temperature is equivalent to increasing the neutral

species number density, which results in increasing the number of particles available for ionization and collisions. The production terms therefore scale linearly with pressure, as do the growth/damping rates (which are given for $\bar{k} = 0$) of the perturbations. Conductivity, however, scales linearly with the collision frequencies, so that for a fixed $\bar{J}/\bar{n}_{e_{ss}}$, the electric field also scales with the charged particle collision frequencies. Hence, at lower pressures, critical conditions occur at lower electric fields than higher pressures. However, we find that the associated growth/damping rates are also smaller,

Pressure (atm)	$T_{e_{crit}}$ (kelvin)	$n_{e_{crit}}$ (m^{-3})	k_{crit} (m^{-1})	λ_{crit} (m)	ω ($k = 0$) (s^{-1})
.1	14500	1.44×10^{19}	2770	2.27×10^{-3}	5.61×10^{6}
.5	14500	1.44×10^{19}	13800	4.55×10^{-4}	2.81×10^{7}
1	14600	1.43×10^{19}	27600	2.28×10^{-4}	5.62×10^{7}
5	14600	1.42×10^{19}	138000	4.55×10^{-5}	2.78×10^{8}
10	14500	1.44×10^{19}	286000	2.20×10^{-5}	5.56×10^{8}

Table 4.1. Effects of varying pressure for T = 6000 K, $J = 1 \times 10^{5}$ A/m^{2}, $\varepsilon_{i} = 13.6$ ev.

signifying that the instability is weaker. For higher pressures, then, the onset of instability may be delayed a small amount, but the instability will be stronger when it occurs. This fact may be more useful when non-linear effects are considered, since these effects are related to the actual magnitudes of the disturbances.

Another parameter which varies with pressure is the critical wavenumber, which increases with pressure. This means that the critical wavelength decreases with increasing pressure, which may also be an important factor to consider when taking into account physical dimensions of plasma devices, as well as the extent to which electrostatic effects contribute. The explanation behind why this happens has to do with the mean free path decreasing with increasing pressure, which affects the distance over which collisional effects are important.

Along with the changes to the critical wavenumber we find that the frequencies associated with these critical conditions also vary with pressure. Table 4.1 shows that these frequencies increase with pressure, beginning from Mhz frequencies at P = .1 atm to 100 Mhz frequencies at 10 atm. This observation may also be an important consideration in finding ways to keep instabilities from forming.

4.7.2.3. Temperature Dependence (P = .5 atm, ε_I=13.6 ev)

We can speculate about the effect of varying heavy species temperature by examining the general conservation equations, eqns. 2.1.1 - 2.1.5. Because the heavy species energy equations are neglected in this study, the heavy species temperature is of secondary interest. The heavy species temperature nevertheless does have an influence in each equation used in this model. In the continuity equation, this temperature affects the neutral species number density, which as we discussed in the previous section affects the generation rate. In the ion momentum equation, its presence is felt in the pressure gradient term. In the electron energy equation, the difference between electron and bulk temperatures helps determine the collisional energy exchange between the two types of particles. And finally, the electron-neutral and ion-neutral momentum exchange frequencies, which affect both the momentum and electron energy equations, depend on the neutral species number density, which again is related to both the temperature and pressure.

The influence of the bulk temperature can be seen in Table 4.2, which describes its effect in terms of the critical electron temperature and electron number density for a fixed current density $J = 1.1 \times 10^5$. The results show that the background temperature does have an effect on the critical conditions; the critical electron temperature and number density both increase slightly with bulk temperature, though the changes are not great. Because of this, $\left(\overline{J} / \overline{n}_{e_{ss}} \right)_{crit}$, and hence $\overline{E}_{crit}$ also increase with bulk temperature, which can be explained by the fact that a stronger field is required to heat the electrons to the critical electron temperature.

T (kelvin)	$T_{e_{crit}}$ (kelvin)	$n_{e_{crit}}$ (m^{-3})	E_{crit} (N/C)	λ_{crit} (m)
4000	14300	1.35×10^{19}	1.09×10^8	3.05×10^{-4}
5000	14400	1.39×10^{19}	9.51×10^7	3.63×10^{-4}
6000	14500	1.45×10^{19}	8.37×10^7	4.33×10^{-4}
7000	14600	1.51×10^{19}	7.40×10^7	4.76×10^{-4}

Table 4.2. Effects of varying background temperature for P = .5 atm, $J = 1 \times 10^5$ A/m^2, $\varepsilon_I = 13.6$ ev.

The bulk temperature also has an effect on the wavenumber at which the instability first appears. With increasing temperature, this critical wavenumber decreases, which indicates that the critical wavelength is increasing. The frequency of these perturbations also change slightly, while remaining at about the same order of magnitude (in the Mhz range).

The analysis in this chapter has provided us with a simplified way to gain insight into the possible mechanisms responsible for instability. By examining this uniform situation first we have examined frequencies, wavelengths, energy equation dependence, the importance of ionization, and introduced the role of phase and amplitude relationships which are also necessary to understand a more realistic stability analysis, as we shall see in the following chapter. In addition, insight into how background conditions affect the results of the analysis has been gained, which again will enhance our approach to interpreting the results of the non-uniform problem.

Chapter 5.

Stability Analysis - Non-Uniform Plasma Case

We now remove the artificial constraint of a uniform plasma and analyze a more physically realistic situation which takes into account the spatially varying background plasma in the electric boundary layer. To accomplish this, we recall the analysis which was discussed in chapter 3, where the steady state profiles for the electric boundary layer were calculated. As outlined in Chapter 2, these conditions are analyzed for stability by modeling the time-dependent response of the boundary layer to small planar perturbations which have the form of Eqn. 2.4.2, which upon substitution results in the perturbation equations 2.3.2 - 2.3.6.

5.1. Additional simplifications

In the actual solution of the non-uniform stability problem, it is very desirable to keep the number of equations as small as possible. One reduction can be made by recalling the far-field boundary condition that all perturbations die out far from the anode, and combining this boundary condition with eqn. 2.3.3 ($\nabla \cdot J = 0$, ignoring two-dimensional effects). This leads to the simple result

$$\hat{\bar{\Gamma}}_e = \hat{\bar{\Gamma}}_i \tag{5.1.1}$$

which states that the perturbation in the overall current density perturbation, $\hat{\bar{J}}$, is not only constant but equal to zero throughout the *entire* boundary layer. Rearranging eqn. 5.1 results in the statement that

$$\hat{\bar{U}}_i = \frac{\overline{U}_{e_{ss}} - \overline{U}_{i_{ss}}}{\overline{n}_{e_{ss}}} \hat{\bar{n}}_e + \hat{\bar{U}}_e \tag{5.1.2}$$

which can then be substituted into the original set to eliminate $\hat{\overline{U}}_i$. The other simplification that can be made is by adding the electron and ion momentum perturbation equations (eqns. 2.3.4 and 2.3.5) to remove the electric field perturbation. The final remaining set thus consists of three equations with three unknowns; the original electron continuity perturbation equation (eqn. 2.3.2), the electron energy perturbation equation (eqn. 2.3.6), and the following statement for the electron velocity perturbation (ignoring electron inertia):

$$-i\overline{\omega}\frac{4}{(1+\mu)\nu_{in}t_R}\overline{n}_{e_{ss}}\left(\hat{\overline{U}}_i+\frac{m_e}{m_i}\hat{\overline{U}}_e\right)=-\frac{d\hat{\overline{n}}_e}{d\overline{x}}-\frac{d}{d\overline{x}}\left(\overline{n}_{e_{ss}}\hat{\overline{T}}_e+\overline{T}_{e_{ss}}\hat{\overline{n}}_e\right)-4\left(\overline{n}_{e_{ss}}\hat{\overline{U}}_e+\overline{U}_{e_{ss}}\hat{\overline{n}}_e\right)$$

(5.1.3)

5.2. Solution method

The actual solution of the eigenvalue problem can be obtained numerically by three different methods: finite differences, the shooting method, or a spectral type method. Simple finite differences are used in this study to discretize the equations and generate the matrix from which the eigenvalues are calculated. The advantages of using the finite difference method are mainly in simplicity and ease of programming. The disadvantages are slow convergence and the return of a large number of "spurious" roots, which are characteristic of the discretization matrix only and have no relation to the physical solution. The number of these spurious roots grows with the size of the matrix, which is a good motivator for reducing the set of equations to the smallest number possible. Distinguishing the physical roots from the spurious roots requires the calculation of eigenvalues from matrices of different sizes (which represent different grid spacings), and finding the eigenvalues which are invariant with grid size (these are the "physical" roots).

Discretization of the domain can be done either with a stretched or uniform grid. In this study, both were used to help confirm the existence of the eigenvalues. Results are given here only for uniform grid calculations.

The discretized form of the three perturbation equations are written for each grid point and form a generalized eigenvalue problem with a coefficient matrix and eigenfunction vector, as discussed in chapter 2. The $\bar{A}$ (coefficient) and $\bar{B}$ matrices, however, are now square matrices with 3N rows and columns, where N is the number of grid points. We note that this will result in much larger matrices than those encountered in the uniform analysis. Numerical solution times of generalized eigenvalue problems scale approximately with N^3, which again reinforces the need for keeping the number of equations and grid points small. In general, the maximum number of eigenmodes calculated is 3N, the size of the matrix; in practice, the actual number of eigenmodes is slightly below this value.

Theoretically, the physical roots should converge to their values as the number of grid points, and hence accuracy, is increased. In this study, the cases are calculated with a certain number of grid points, and then re-calculated with twice as many grid points as before. Physical eigenvalues should be revealed for both cases and be fairly equal, showing a pattern of convergance with decreasing mesh size. Spurious eigenvalues will not display this type of behavior, and also will tend to have the additional characteristic that their eigenfunctions display strong spatial variations which bear a resemblance to so-called "noise" plots.

The three perturbation equations represent a fourth order set of linear ordinary equations, which require four boundary conditions for solution. As discussed in Chapter 2, we require that $\hat{\bar{n}}_e$, $\hat{\bar{U}}_e$, and $\hat{\bar{T}}_e$ dissapear in the far-field. The remaining boundary equation is the enforcement of eqn 2.6.1, the recombination boundary condition at the anode. The perturbation form of this boundary condition, obtained by the usual method of substituting the sum of steady state and perturbation quantities, is

$$-2k_{si}\bar{n}_{e_{ss}}\hat{\bar{n}}_e = \bar{U}_{e_{ss}}\hat{\bar{n}}_e + \bar{n}_{e_{ss}}\hat{\bar{U}}_e \tag{5.2.1}$$

at the anode wall. We note that it is not necessary to include the questionable condition of a zero gradient for the electron temperature perturbation at the anode for this non-uniform analysis.

5.3. Results

5.3.1 High current case, unstable mode

The conditions which we examine for stability are again those given in Table 3.1, supporting a non-dimensional current density of $\bar{J} = 40$, which corresponds to a dimensional current density of $\bar{J} = 1.1 \times 10^4 \, \text{A/m}^2$. The boundary layer profiles for these conditions are also presented in Chapter 3. The current density chosen was identified in Eskin's thesis as an approximate transition point from the diffuse mode to the constricted mode, though it is not stated where this value originates from. At higher current densities, the eigenfunction gradients are sharper and hence a greater spatial resolution is needed to accurately resolve them.

Performing the calculations using a uniform grid with 100 grid points, over a domain from $\bar{x} = 0$ to $\bar{x} = .03$, we find that the resulting eigenvalues span over a wide range of values. A significant number of these eigenvalues are not realistic because they have (dimensional) real components which are smaller than 10^{-10} seconds, which is on the order of a 100 year period! These roots are clearly spurious and can immediately be discarded. The remaining set of eigenvalues, which still contain some spurious modes, are displayed on a log-log scale of their imaginary vs. real parts in Fig. 5.1.

We first note that the Fig. 5.1 is symmetric about the ω_r axis. The eigenvalues which differ only by a sign in the real part actually represent the same mode. Another thing to note is that there are quite a few roots where $\bar{\omega}_r$ lies in the 10^6-10^8 range for which ω_i is positive. A discussion of these roots will follow; we will first focus our attention on the lone root where $\bar{\omega}_r$ lies in the 10^4 range and has a positive imaginary component. This root has a calculated eigenvalue of $\bar{\omega} = 3.75 \times 10^4 + 1.32 \times 10^4 i$ for 100

grid points. Repeating the calculation with 200 grid points reveals that the root takes on a value of $3.85 \times 10^4 + 1.26 \times 10^4 i$, and with 300 grid points (which takes about a full day to run on a Sun Sparc 20 workstation), $\overline{\omega} = 3.91 \times 10^4 + 1.23 \times 10^4 i$, which indicates fairly
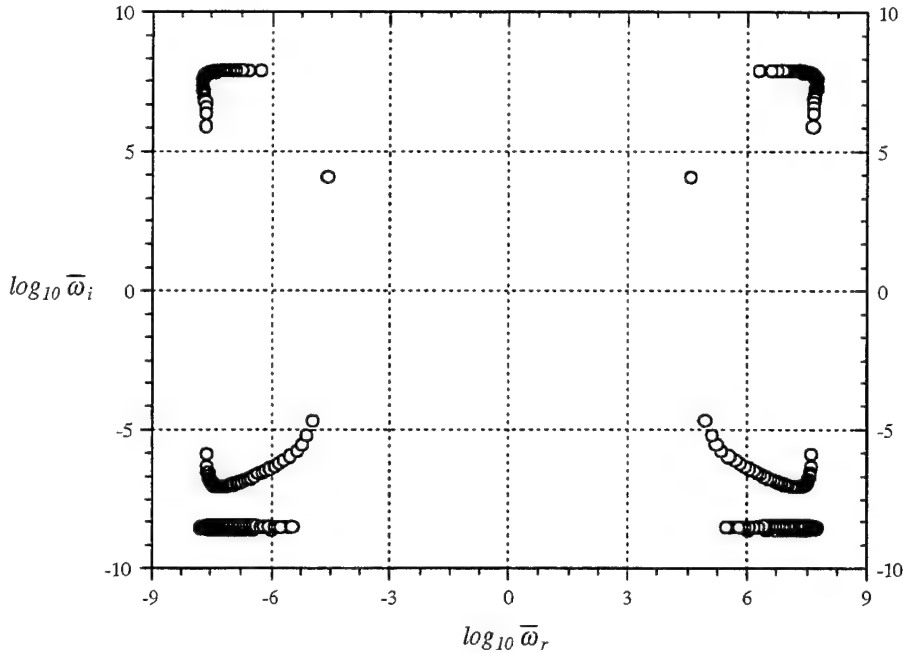

Figure 5.1. Log-log plot of the real vs. the imaginary parts of the eigenvalues for 100 grid points.

good convergance. We will take this as an indication that the root is not spurious and hence physical. It should be noted that the dimensional value of the frequency $(\omega_r = \overline{\omega}_r / t_R)$ for this unstable eigenvalue is around 10^6 s^{-1}, or about 1 Mhz.

Examination of the eigenfunctions of this unstable mode provides insight on how the perturbations vary spatially. The amplitude of the eigenfunctions of the three parameters which are directly calculated - n_e, U_e, and T_e - are given in Fig. 5.2 for the 200 grid point calculation, with every other data point (100 points total) plotted to reduce clutter. Each eigenfunction amplitude is normalized with its maximum value so that the three may be plotted on the same graph for comparison. We find that the electron

velocity and temperature amplitudes show a smooth, almost exponential, decay towards zero, with the velocity exhibiting a shorter scale length than the temperature. The number density amplitude shows a maximum near the anode before its smooth decay, which may be a result of the finite rate recombination boundary condition (eqn. 5.2.1). The eigenfunction amplitudes of the properties which are "backed out" after the main problem is solved - $\hat{\overline{U}}_i$, $\hat{\overline{E}}$ - as well as illustrative properties such as the electron/ion flux, $\hat{\overline{\Gamma}}_j$, and flux gradient $d\hat{\overline{\Gamma}}_e / d\overline{x}$ perturbations - are shown in Figs. 5.3 and 5.4, respectively. The relative phase plots of all of these eigenfunctions are given together in Fig. 5.5.

We see from these plots that near the anode, the eigenfunctions for the ion velocity and electron flux are not very smooth, and are characterized by steep gradients which appear as discontinuities because of the grid scale used. This is again due to the finite rate recombination boundary condition imposed at the anode. Written in another way, it imposes that

$$\left(-2k_s\overline{n}_{e_{ss}} - \overline{U}_{i_{ss}}\right)\hat{\overline{n}}_e = \overline{n}_{e_{ss}}\hat{\overline{U}}_i \tag{5.3.5}$$

at $\overline{x} = 0$. This, along with eqn. 5.1.1, are statements that attempt to model the effect of the anode while maintaning the one-dimensional and quasineutral simplifications. However, this is physically unrealistic because of the existence of a sheath in front of the anode. When electrostatic and two-dimensional effects are taken into account, there is no longer the requirement to set the electron and ion flux perturbations equal to each other. Also, the use of a single recombination coefficient to describe the highly complex anode-plasma interaction is a gross simplification. In order to more realistically treat the problem, the ion and electron flux should be decoupled, and separate reaction rate coefficients, each with their own dependencies on temperature and number density, should be used to describe specific reactions, in addition to taking two-dimensional and electrostatic effects into account. However, while acknowledging the shortcomings of
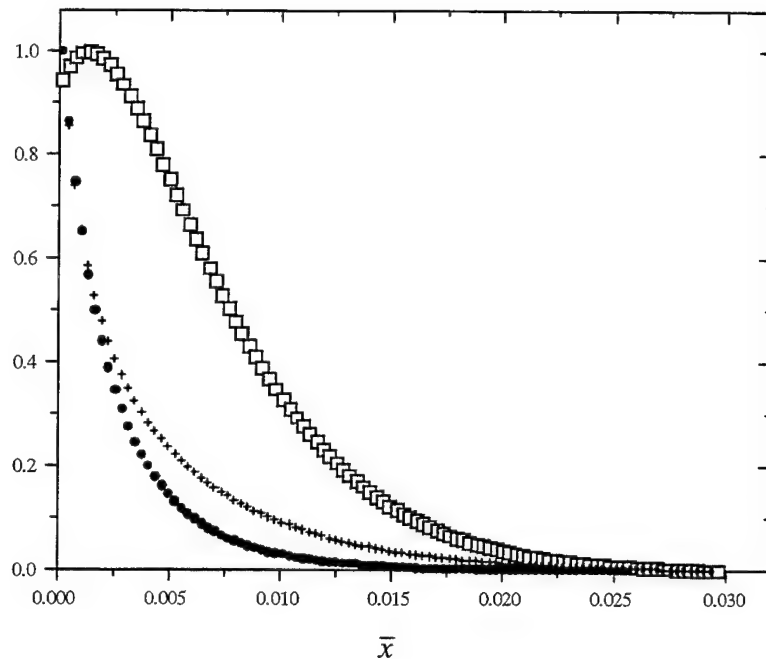
Figure 5.2. Normalized Amplitudes for the eigenfunctions $\hat{\bar{n}}_e$ ($\square$), $\hat{\bar{U}}_e$ ($\bullet$), $\hat{\bar{T}}_e$ (+). The maximum values of the amplitudes are 1.88×10^{-7}, 0.353, and 3.52×10^{-6}, respectively.
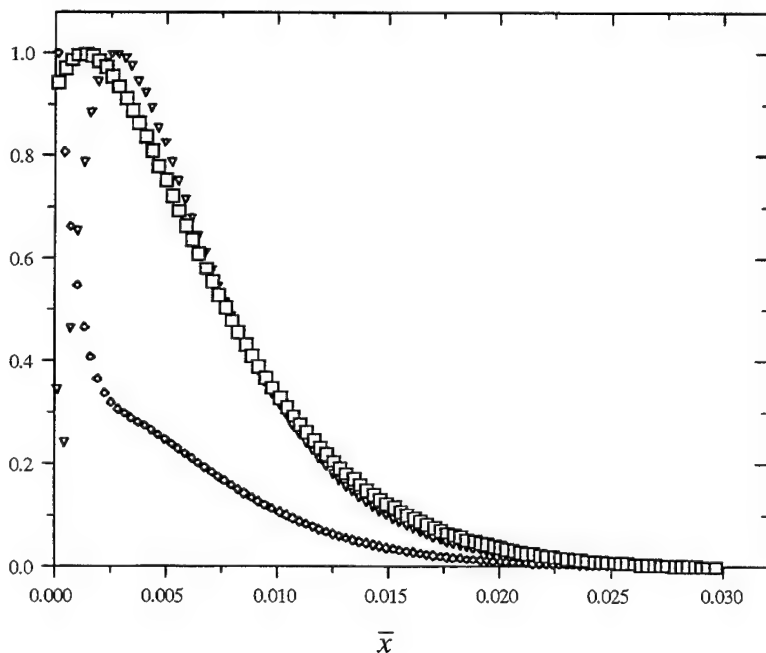
Figure 5.3. Normalized Amplitudes for the eigenfunctions $\hat{\bar{n}}_e$ ($\square$), $\hat{\bar{U}}_i$ ($\triangledown$), $\hat{\bar{E}}$ ($\lozenge$). The maximum values of the amplitudes are 1.88×10^{-7}, 1.33×10^{-4}, and 8.91×10^{-4}, respectively.
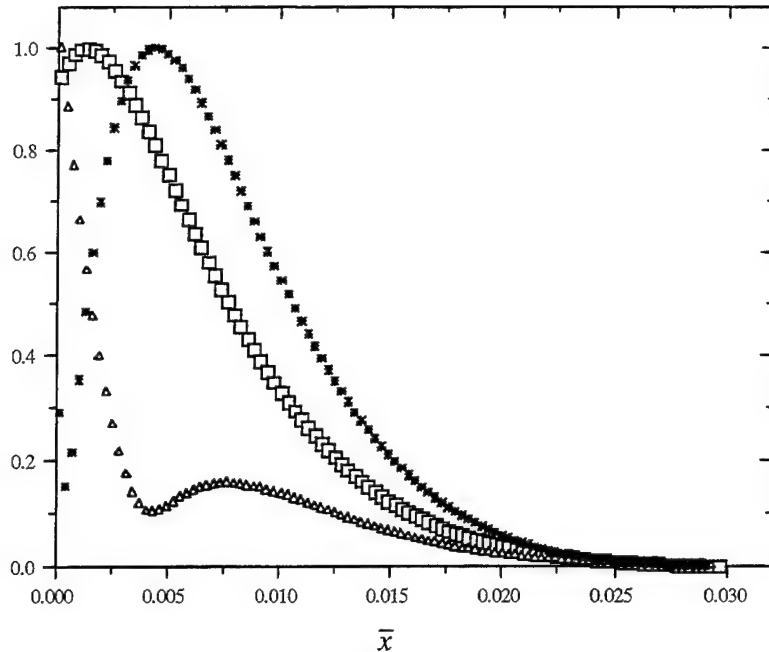
Figure 5.4. Normalized Amplitudes for the eigenfunctions $\hat{\bar{n}}_e$ ($\square$), $d\hat{\bar{\Gamma}}_e / d\bar{x}$ ($\triangle$), $\hat{\bar{\Gamma}}_e$ (*). The maximum values of the amplitudes are 1.88×10^{-7}, 1.33×10^{-4}, and 8.91×10^{-4}, respectively. Note the discontinuity in the flux amplitude at the anode wall.
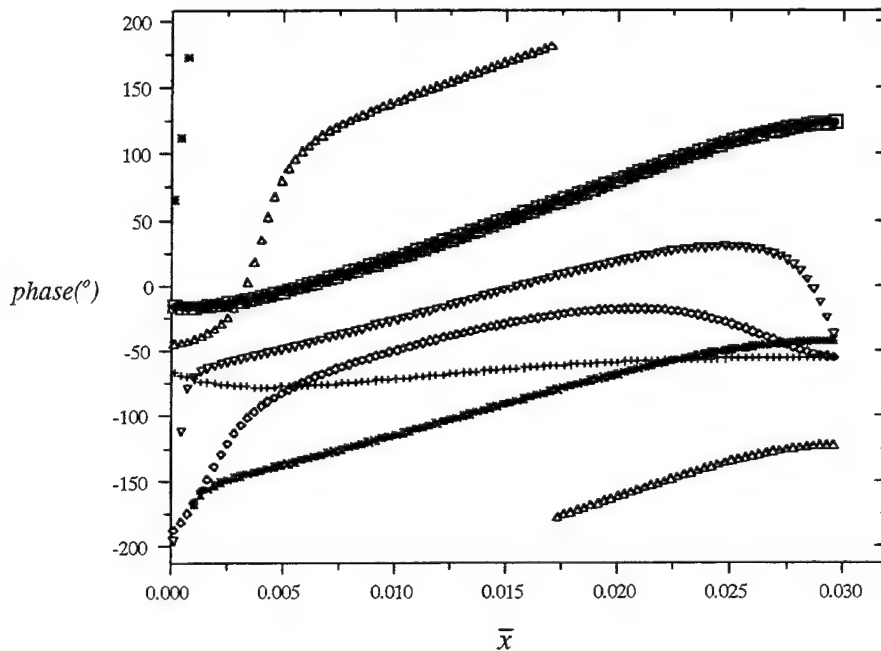
Figure 5.5 . Relative phase (in degrees) for the eigenfunctions $\hat{\bar{n}}_e$ ($\square$), $\hat{\bar{U}}_e$ ($\bullet$), $\hat{\bar{T}}_e$ (+), $\hat{\bar{U}}_i$ ($\triangledown$), $\hat{\bar{E}}$ ($\lozenge$), $d\hat{\bar{\Gamma}}_e / d\bar{x}$ ($\triangle$), $\hat{\bar{\Gamma}}_e$ (*). Note that the electron density and velocity perturbations are approximately in phase.

eqn. 5.2.4, we will still rely on it to model the anode boundary condition in a mathematically simple way.

The discontinous behavior of the ion velocity and flux near the anode disappears for low values of k_{si}. This can be seen in eqn. 5.3.5, where higher values of k_{si} force the ion velocity and electron number density to be 180 degrees out of phase. In the limit of setting k_{si} to zero, the ion flux perturbation is forced into phase with the number density perturbation (because the steady ion velocity at the anode is negative for non-saturated cases), which gives the ion velocity eigenfunction a smoother variation and removes the steep gradient behavior in the ion velocity amplitude. In the limit of the one-dimensional quasineutral model, it seems that the ion velocity and flux are better behaved near the anode for low values of k_{si}, which physically corresponds to lower steady state ion fluxes at the anode (closer to saturation conditions).

At a small distance away from the anode, we find that every one of the eigenfunctions are well behaved. The electron velocity disturbance amplitude is many orders of magnitude greater than that of the ions, which as we saw in Chapter 4 indicates that this is not an "ion" type disturbance. The phase of the electron number density and velocity are very nearly (but not exactly) equal. If they were exactly equal, the ion velocity perturbation would be either in phase or 180 degrees out of phase with these two properties (as seen by eqn. 5.1.2), which is not the case. The phase of the electron number density perturbation also does not change very rapidly, making a 90 degree change from the anode to approximately $\bar{x} = .02$, where its amplitude has almost died out. This shows that the number density perturbation does not exhibit a strong spatial oscillation, and that the perturbation is mostly monotonic. This observation may be important when considering the non-linear processes of arc transition. We will see that for another set of conditions (the low current density case) the number density phase has a stronger spatial variance, which essentially divides the disturbance into regions where the electron number density perturbations are negative and positive.

A physical explanation for the instability exhibited by this mode can be deduced by examining the nature of the steady state boundary layer. By considering electron particle conservation, we recall that the steady state boundary layer is in a state of charged particle production, which is balanced out by the flux gradients which carry the produced particles towards the anode, where they recombine. By first assuming for the moment that the steady state production rate is fixed (that is, $\hat{\bar{n}} = 0$), it is possible to hypothesize that a perturbation to the overall flux of charged particles, perhaps due to a fluctuation in the electric field, can upset the particle balance and result in a build-up of charged particles in the region. This process could then conceivably lead to a local increase in conductivity, which has been speculated as the transition initiating mechanism in electrothermal instability theory.

This flux instability mechanism can also be aided by $\hat{\bar{n}}$. For the case under consideration, a perturbation to the overall electron/ion flux results in a positive perturbation to the charged particle number density, which grows due to a combination of the flux disturbance and increase in particle production. Important physical insight can be gained by examining eqn. 2.4.3 (the continuity perturbation equation). From this equation we conclude that the perturbation flux gradient is a major factor in determining the growth or decay characteristics of the disturbance. By comparing the eigenfunctions of the electron number density and flux gradient (which is calculated by a simple difference formula), we can determine the role that the flux gradient is playing in the instability. Fig. 5.4 shows that the two eigenfunctions start out relatively in phase, and actually come into phase at $\bar{x} \sim .0025$. In this region, the flux perturbation gradient is acting to damp out the disturbance by moving particles out of this near anode region. However, there is a contribution to the growth of the number density perturbation from $\hat{\bar{n}}$, which maintains the instabililty in this region. The "production coefficient," which was introduced in the previous chapter, is fairly high (about 10^4) here and thus indicates that many additional particles are being rapidly produced in the region due to perturbations in electron density and temperature. Further away from the anode, where the production coefficient is smaller, the two eigenfunctions go out of phase by about

120 degrees, indicating that the flux gradient begins to aid the instabilty. A relative phase of 180 degrees would indicate that the flux gradient is purely growth term, though anything from 90 to 270 degrees indicates a net influx of particles and hence a partial role as a growth mechanism.

This characterization of the instability as a "flux" instability is something that was not exhibited in the previous "quasi-uniform" analysis. We recall in that analysis that the steady state flux gradients were ignored, which prevented the flux perturbation from becoming a major factor in determining stability characteristics. Instability was related to the electron energy equation as a disruption to the energy balance of Joule heating, pressure work and conduction, which are more closely tied with electrothermal instability theory. In the present non-uniform analysis, the electron energy equation does not appear to be the deciding factor in determining the instability of the boundary layer. Hence, it seems that net ionization rate, rather than current density, is the important factor in current stability. This is reinforced by the following case, which is a stability analysis of a very low current boundary layer in the state of Joule cooling.

5.3.2. Low current case, unstable mode

The steady state profiles for a boundary layer with the same conditions as the previous case, with the exception that $\bar{J} = .4$ (about 110 A/m^2), are also given in figs. 3.1 - 3.8. For this case we find that the steady state electron temperature falls as the anode is approached, indicating a negative electric field and the boundary layer being in a state of "Joule cooling". Despite this fact, the boundary layer is still in a state of ionization, although the production rates are much lower than in the previous case. Again we can imagine a flux perturbation in this boundary layer which can cause the number density of the electrons and ions to grow, though we would expect the growth to be weaker. The stability analysis reveals the existence of an unstable mode with $\bar{\omega} \approx 1.9 \times 10^4 + 4.4 \times 10^3 i$, which has a growth rate about a factor of 3 smaller than the $\bar{J}$ = 40 case. Figs. 5.6 - 5.9 show the plots of the eigenfunction amplitudes and phase

relationships, in a format similar to those given for the higher current case. We find that while there are similarities, there are also some distinguishing characteristics for this low current mode which could potentially be important when considering the dynamics of anode spot formation.

It is obvious by considering the steady state temperature profile that the production coefficient is always going to be very close to unity. Hence, the production perturbation $\hat{\tilde{n}}$ is not going to have a strong influence on any instability. If a mode is going to be unstable, it should be entirely due to the flux perturbation. This fact is confirmed by examining the phase plot for this case, which shows that the relative phase between the electron number density and flux gradient perturbations is always greater than 90 degrees.

Another interesting difference for this case is that the phase of the number density perturbation changes very rapidly near the anode, making a 180 degree change from the anode at $\bar{x} = .01$. This is in contrast to the higher current case, where the number density phase did not vary significantly past 90 degrees. This indicates that, for this low current case, the number density perturbation has more of a spatially wave-like character, where regions are divided into positive and negative perturbations. Physically, this signifies that charged particles are initially only being shuffled around by the disturbance, and that there are very few new particles being produced. These characteristics may have important implications when considering transition dynamics, though any further conclusions would require verification from more complex models.

We note that for this low current case, we do not see the discontinous behavior of the ion velocity and electron flux which was found in the previous case. This is due to the fact that for a large portion of the boundary layer, the steady state ion velocity is negative, resulting in a more continuous variation for the eigenfunctions in question.
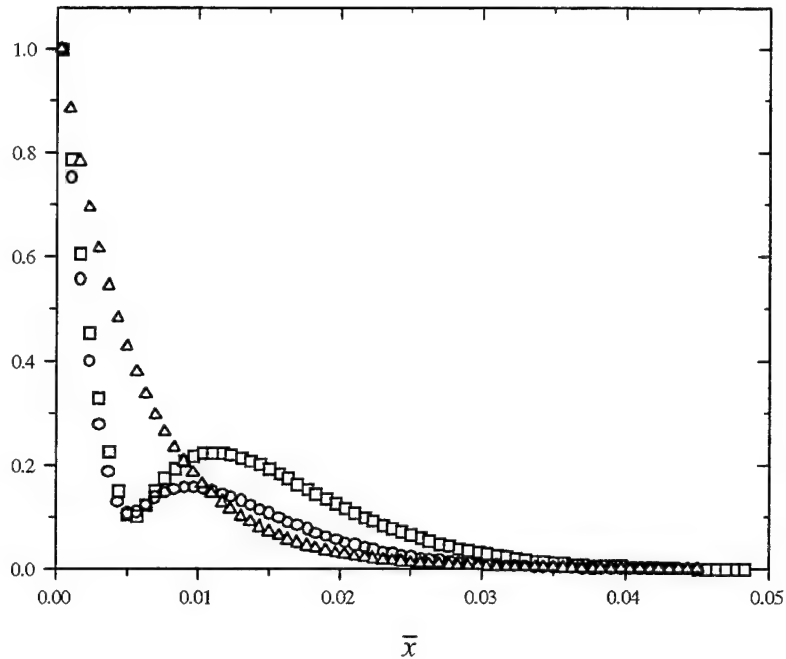
Figure 5.6. Normalized Amplitudes for the eigenfunctions $\hat{\bar{n}}_e$ ($\square$), $\hat{\bar{U}}_e$ ($\circ$), $\hat{\bar{T}}_e$ (Δ). The maximum values of the amplitudes are 1.09×10^5, 0.471, and 1.72×10^3, respectively.
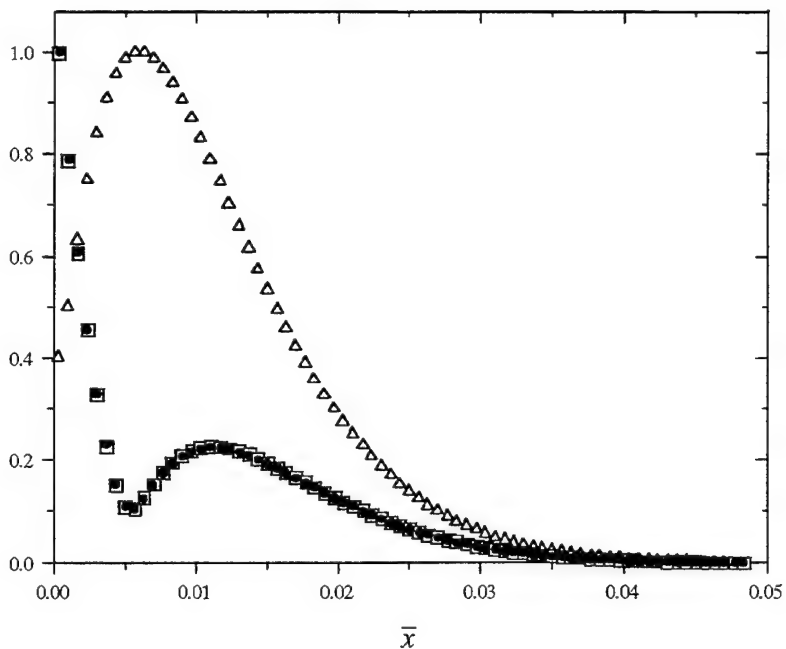
Figure 5.7. Normalized Amplitudes for the eigenfunctions $\hat{\bar{n}}_e$ ($\square$), $d\hat{\bar{\Gamma}}_e / d\bar{x}$ ($\bullet$), $\hat{\bar{\Gamma}}_e$ (Δ). The maximum values of the amplitudes are 1.09×10^5, 0.21, and 6.11×10^4, respectively.
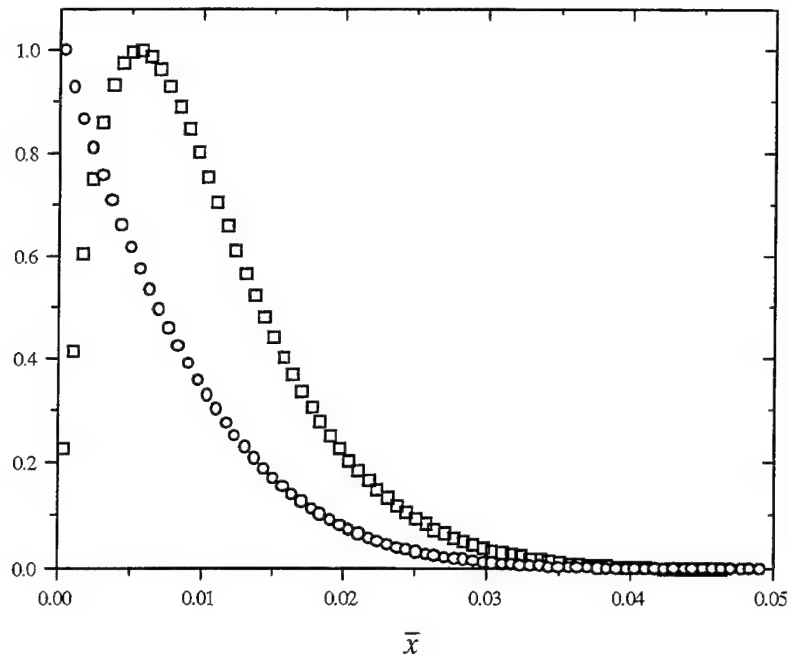
Figure 5.8. Normalized Amplitudes for the eigenfunctions $\widehat{\overline{U}}_i$ ($\square$), $\widehat{\overline{E}}$ ($\circ$). The maximum values of the amplitudes are 1.55×10^{-2} and 0.131, respectively.
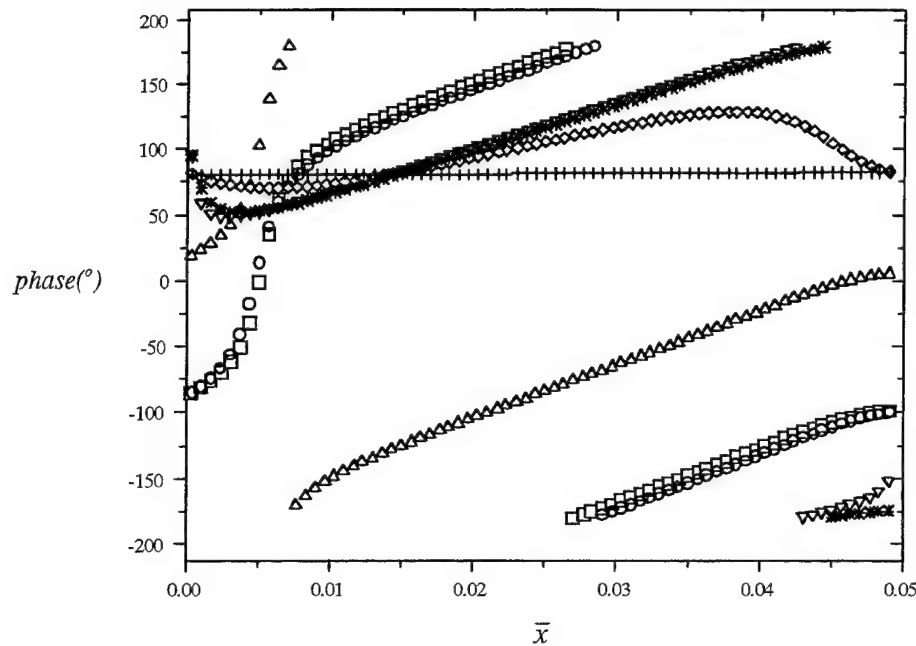
Figure 5.9. Relative phase (in degrees) for the eigenfunctions $\widehat{\overline{n}}_e$ ($\square$), $\widehat{\overline{U}}_e$ ($\circ$), $\widehat{\overline{T}}_e$ (+), $\widehat{\overline{U}}_i$ ($\triangledown$), $\widehat{\overline{E}}$ ($\lozenge$), $d\widehat{\overline{\Gamma}}_e / d\overline{x}$ ($\triangle$), $\widehat{\overline{\Gamma}}_e$ (*). Note that the electron density and velocity perturbations are approximately in phase.

The results of the low current case seem to indicate that, for this particular mode, the electric boundary layer instability is based at least partially on the upsetting of the balance of steady state charged particle production and flux. Joule heating seems to have a very minor, if any, role in the stability characteristics. This fact is confirmed by the fact that raising the current density by an order of magnitude also has a relatively minor effect on the growth rate. Specifically, a stability analysis for the $\bar{J} = 400$ case shows that $\bar{\omega} \approx 4.0 \times 10^4 + 1.38 \times 10^4 i$ for this mode, which does not indicate a significant increase in growth rate from the $\bar{J} = 40$ case. Part of the reason for this is that the peak steady state electron temperature (which occurs at the anode) is 1.83, as opposed to 1.76 for the $\bar{J} = 40$ case. Hence, the steady state production rate $\dot{n}$ and the production coefficient do not increase very significantly from increasing the current density by an order of magnitude. For boundary layers which do have a strong current density to ionization rate relationship, however, we might expect a stronger correlation between the current density and the growth rate to exist.

5.3.3. Other modes

As mentioned previously, the stability analysis of all current densities discussed so far turned up a number of eigenvalues which also had positive imaginary values. It is difficult to say whether these modes, which have non-dimensional frequencies and growth rates on the order of 10^7, are physical. This is because the eigenfunctions show very sharp gradients throughout the entire region, with many modes exhibiting a very "noisy" pattern. The number of grid points needed to properly resolve such gradients is large and are very numerically expensive to calculate. As a result, to keep within the scope of this study, we will not focus any more attention on these modes. Their steep gradients and non-convergance give serious doubts to their existence, and more elaborate methods are needed to analyze them to determine if they are indeed physical.

We now turn our attention to the examination of the stable modes. Moving up in frequency from the physical unstable mode discussed earlier, there exist a set of

eigenfunctions with non-dimensional frequencies and damping rates in the 10^5 range, about an order of magnitude greater than the unstable mode. As an illustrative example, we choose to examine a mode where $\overline{\omega} \approx 1.65 \times 10^5 - 3.29 \times 10^5 i$, which has its eigenfunction amplitudes and phases plotted in Figs. 5.10 - 5.13. From these plots it can be seen that at these higher frequencies, some of the eigenfunctions display a more spatially oscillating character. This is illustrated by the changes and periodic variations of the perturbation phase. A perfectly straight phase line would correspond to an exact sinusoidal variation in space. The amplitude plots seem to indicate a "beat" behavior in some of the eigenfunctions. An interesting thing to note is that for a certain region of the boundary layer ($\overline{x} > .0075$), the flux gradient perturbation is almost exactly in phase with the number density perturbation. This helps explain why the mode is stable, though we suspect that the spatially oscillating character of the eigenfunction also plays a strong role. Again, it should be noted that none of the eigenfunctions suffer from any discontinuities.

The remaining type of eigenmode that can be resolved occurs for eigenvalues with damping rates very close to 3×10^8, which is a strong indication that these are "ion" type disturbances first encountered in the uniform analysis. Examination of the eigenfunctions for these modes again strengthen the notion that the higher frequency modes tend to be strongly oscillating "noise" plots which we cannot comment any further on. Lower frequency ion modes, however, are very well behaved. An example of this is the mode corresponding to $\overline{\omega} \approx 7.05 \times 10^5 - 3.0 \times 10^8 i$, which is plotted in Figs. 5.14 - 5.17. A comparison of the ion and electron velocity magnitudes shows that their amplitudes are very nearly equal, confirming the notion that this disturbance is dominated by ion momentum. Fig. 5.17, which displays the relative phase plot, clearly indicates by the linear variation that all of the eigenfunctions are sinusoidal. This figure also shows that the number density and flux gradient perturbations are almost exactly in phase, which helps explain the stability properties of the mode.
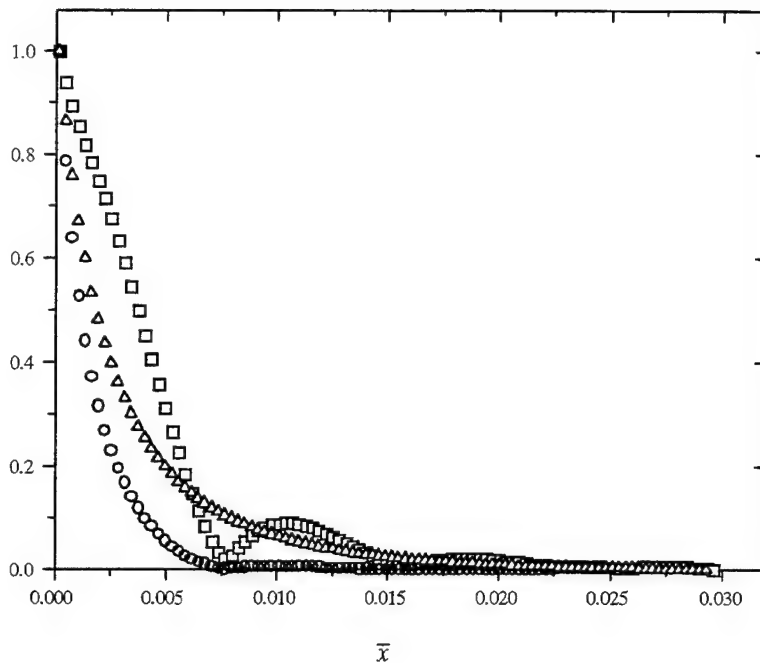
Figure 5.10. Normalized Amplitudes for the eigenfunctions $\hat{\bar{n}}_e$ ($\square$), $\hat{\bar{U}}_e$ ($\bigcirc$), $\hat{\bar{T}}_e$ ($\triangle$). The maximum values of the amplitudes are 2.16×10^{-7}, 0.428, and 2.00×10^{-5}, respectively.
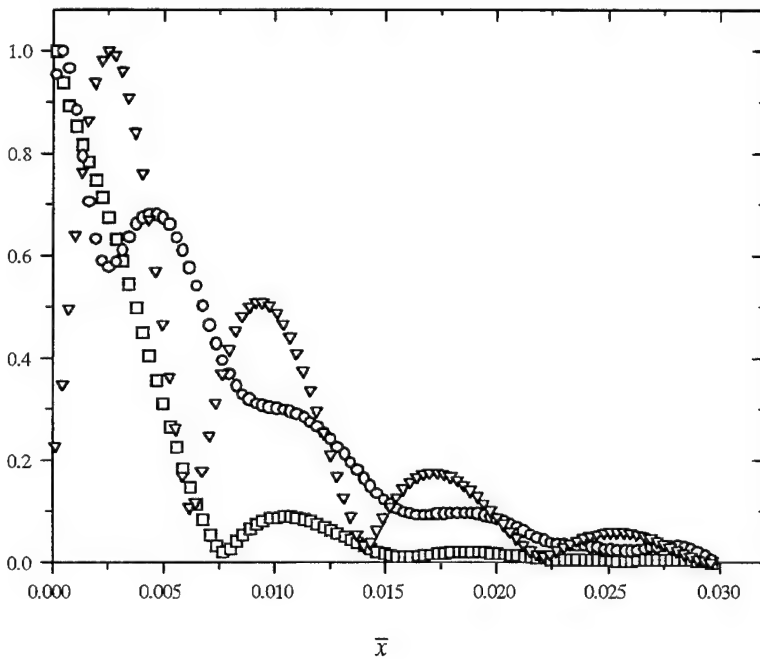
Figure 5.11. Normalized Amplitudes for the eigenfunctions $\hat{\bar{n}}_e$ ($\square$), $d\hat{\bar{\Gamma}}_e / d\bar{x}$ ($\bigcirc$), $\hat{\bar{\Gamma}}_e$ (∇). The maximum values of the amplitudes are 2.16×10^{-7}, 1.57×10^{-2}, and 2.54×10^{-5}, respectively.
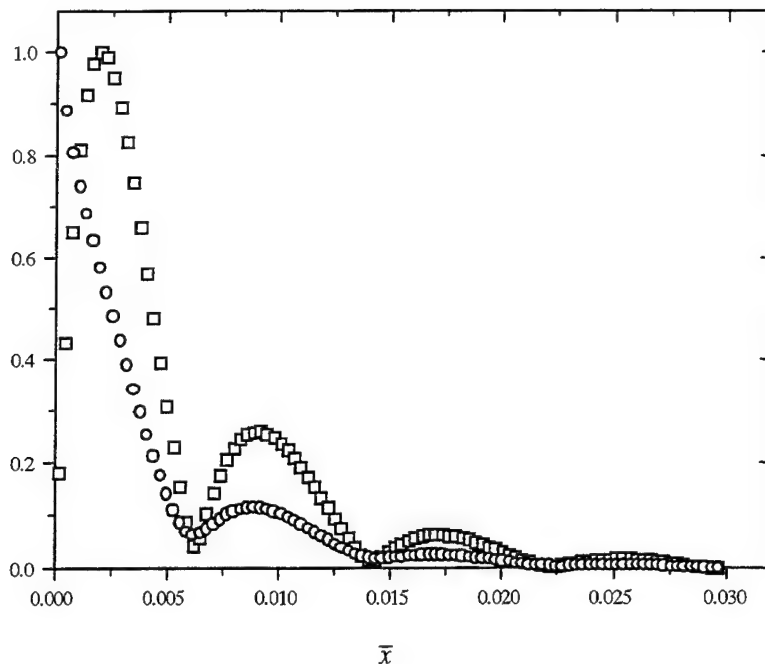
Figure 5.12. Normalized Amplitudes for the eigenfunctions $\hat{\overline{U}}_i$ ($\square$), $\hat{\overline{E}}$ ($\bigcirc$). The maximum values of the amplitudes are 3.06×10^{-4} and 2.44×10^{-3}, respectively.
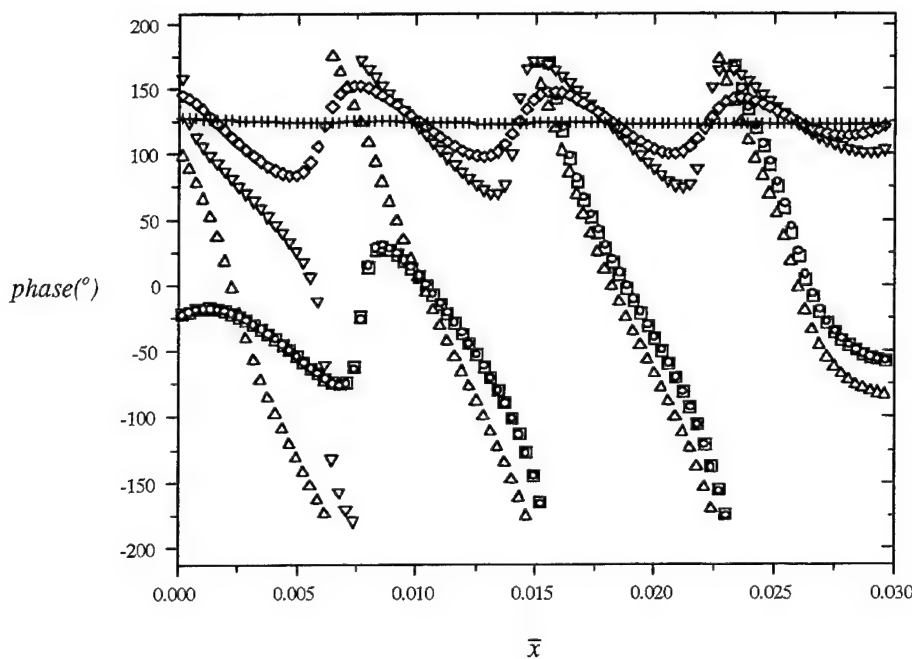
Figure 5.13. Relative phase (in degrees) for the eigenfunctions $\hat{\overline{n}}_e$ ($\square$), $\hat{\overline{U}}_e$ ($\bigcirc$), $\hat{\overline{T}}_e$ (+), $\hat{\overline{U}}_i$ ($\triangledown$), $\hat{\overline{E}}$ ($\lozenge$), $d\hat{\overline{T}}_e / d\overline{x}$ ($\triangle$). Note that the electron density and velocity perturbations are approximately in phase, and that phase of $\hat{\overline{T}}_e$ is not plotted because it has the same phase as the ion velocity perturbation.
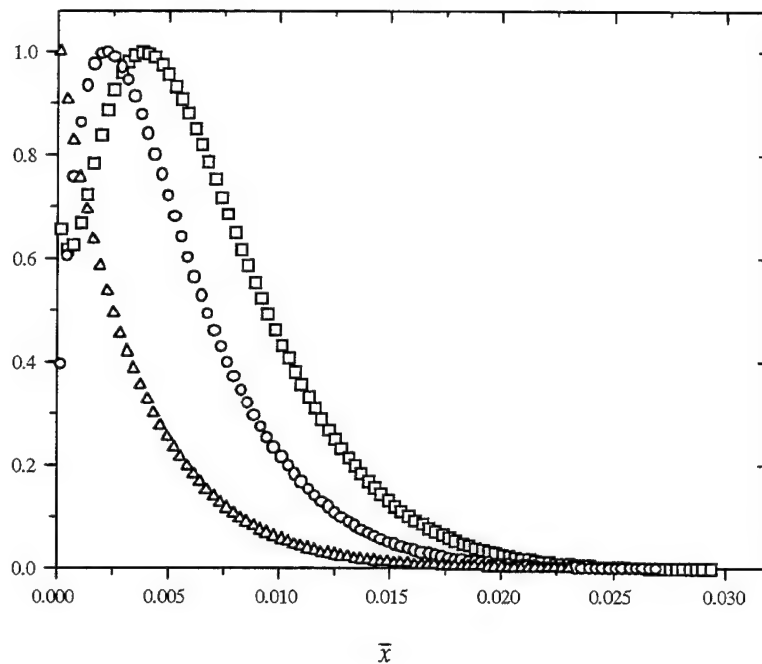
Figure 5.14. Normalized Amplitudes for the eigenfunctions $\hat{\bar{n}}_e$ ($\square$), $\hat{\bar{U}}_e$ ($\circ$), $\hat{\bar{T}}_e$ ($\triangle$), ion mode. The maximum values of the amplitudes are 1.09×10^{-5}, 0.471, and 1.72×10^{-3}, respectively.
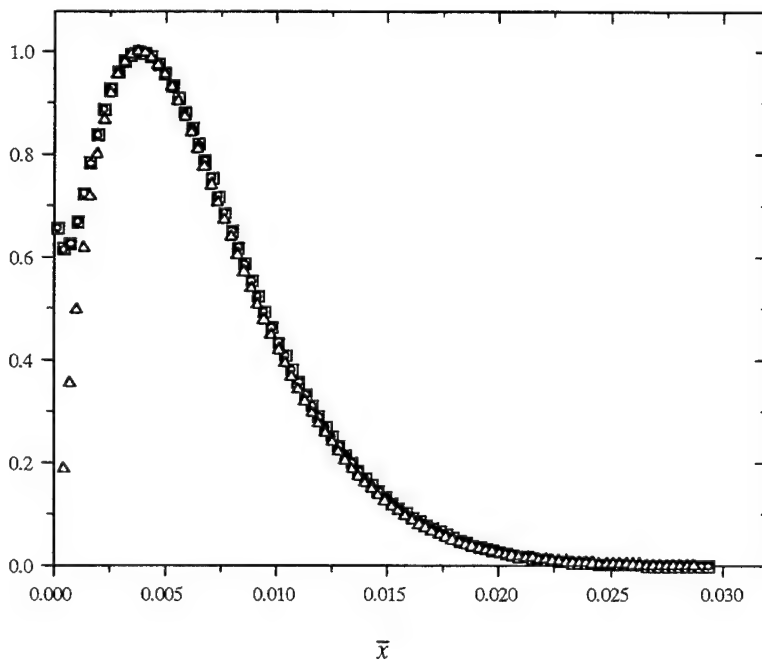
Figure 5.15. Normalized Amplitudes for the eigenfunctions $\hat{\bar{n}}_e$ ($\square$), $d\hat{\bar{T}}_e / d\bar{x}$ ($\circ$), $\hat{\bar{T}}_e$ ($\triangle$), ion mode. The maximum values of the amplitudes are 1.09×10^{-5}, 0.21, and 6.11×10^{-4}, respectively.
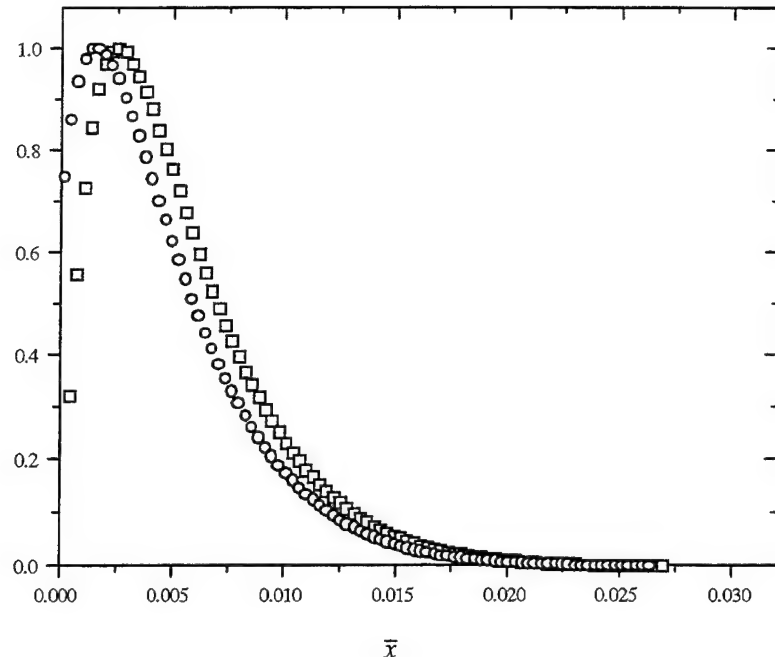
Figure 5.16. Normalized Amplitudes for the eigenfunctions $\widehat{\overline{U}}_i$ ($\square$), $\widehat{\overline{E}}$ ($\circ$), ion mode. The maximum values of the amplitudes are $1.55\mathrm{x}10^{-2}$ and .131, respectively.
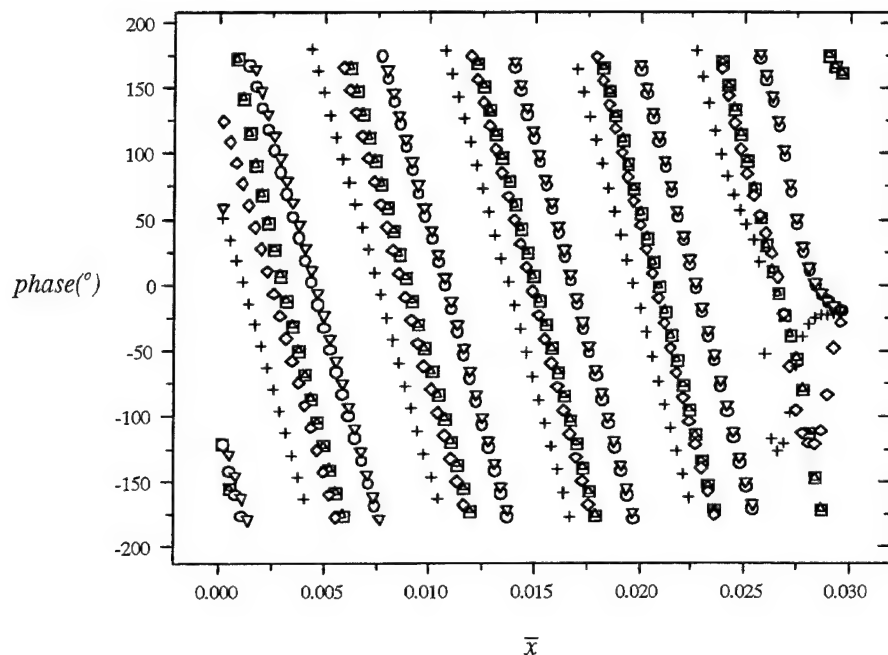
Figure 5.17. Relative phase (in degrees) for the eigenfunctions $\widehat{\overline{n}}_e$ ($\square$), $\widehat{\overline{U}}_e$ ($\circ$), $\widehat{\overline{T}}_e$ (+), $\widehat{\overline{U}}_i$ ($\triangledown$), $\widehat{\overline{E}}$ ($\lozenge$), $d\widehat{\overline{T}}_e / d\overline{x}$ ($\triangle$), $\widehat{\overline{\Gamma}}_e$ (*), ion mode. Note that the electron density and velocity perturbations are approximately in phase.

It is interesting to note that among the different modes, the electron temperature perturbation maintains a fairly consistent quality. This could possibly be interpreted as additional evidence that the electron energy equation does not have a large role to play in the stability characteristics of the electric boundary layer.

5.4. Model Limitations

Because of the short length scales which characterize the perturbations, we must be aware of the quasineutral limitations of our model. We have already discussed the possible effects of the sheath on the anode boundary conditions in a previous section. We must also consider whether Poisson's equation (eqn. 2.1.6), and hence quasineutrality, is being violated by the perturbations. The condition for satisfying Poisson's equation for the perturbations is:

$$z\varepsilon^2 \frac{d\hat{\bar{E}}}{d\bar{x}} << z\hat{n}_e \tag{5.4.1}$$

where the parameter z is used to illustrate that the perturbation vector $\bar{y}$ represents a linear "basis" vector for the domain of allowable perturbations. However, it is clear that z drops out and has no effect in this analysis, which allows the usage of any convenient perturbation value to determine the applicability of the quasineutral assumption.

As a rough approximation, we can use the perturbation magnitudes to give an order of magnitude "test" for Poisson's equation. For our current case, we find that ε has a value of 4.6×10^{-5}, and that the scale length of the electric field perturbation can be very conservatively estimated to be 0.001. Substituting the maximum values for the electric field and electron number density perturbations, we find that the left hand side of eqn 5.4.1 is about 1% the value of the right hand side, which indicates that quasineutrality seems to be reasonably satisfied for these perturbations.

We must always be aware that our assumption of a one-dimensional problem also introduces approximations. However, a more rigorous two-dimensional treatment brings a whole host of theoretical and numerical complications. To help understand the approximations being made with the 1-D assumption, we examine the differential form of Ampere's Law:

$$\nabla \times \vec{B} = \mu_0 \left(\vec{J} + \varepsilon_0 \frac{\partial \vec{E}}{\partial t} \right)$$

(5.4.2)

Taking the divergance of both sides gives

$$\nabla \cdot \vec{J} = -\varepsilon_0 \frac{\partial}{\partial t} \left(\nabla \cdot \vec{E} \right)$$

(5.4.3)

Expanding this into 2-D form by assuming radial symmetry, we get

$$\frac{1}{r} \frac{\partial}{\partial r} \left(r J_r \right) + \frac{\partial J_x}{\partial x} = \frac{\partial}{\partial t} \left[\frac{1}{r} \frac{\partial}{\partial r} \left(r E_r \right) + \frac{\partial E_x}{\partial x} \right]$$

(5.4.4)

In laboratory situations, we expect that in general, real perturbations will have multi-dimensional components. However, for our idealized model of perfectly planar perturbations, we can neglect the radial terms. Hence, after non-dimensionlization and applying perturbations, we are left with

$$\frac{\partial}{\partial x} \left(\hat{\tilde{\Gamma}}_i - \hat{\tilde{\Gamma}}_e \right) = \frac{\left(1 + \mu \right)^2}{4\mu} \frac{\varepsilon_0}{t_R \sigma_R} i\omega \frac{\partial \hat{\tilde{E}}_x}{\partial x} e^{-i\omega t} \approx 2 \times 10^{-9} i\omega \frac{\partial \hat{\tilde{E}}_x}{\partial x} e^{-i\omega t}$$

(5.4.5)

for the conditions stated in Table 3.1. Using an order of magnitude estimate and assuming that the gradients on both sides of the equation have the same scale length of

variation, we can get an estimate of the frequency for which there exists a net current perturbation (when the right hand side of the equation is not negligible) as

$$|\overline{\omega}|_{max} \approx 5 \times 10^{-8} \frac{\left|\hat{\overline{\Gamma}}_e\right|_{max}}{\left|\hat{\overline{E}}\right|_{max}} \approx 10^7 \tag{5.4.6}$$

which is satisfied for the unstable mode described in section 5.3.1.

5.5. The role of the boundary layer character on stability

It is apparent from the analysis presented that the model lacks the ability to define a boundary, or demarcation point, between conditions of stable and unstable behavior for the situation described. Differences in mode structures can be examined to speculate their effects on current mode transition; however, the task of testing such speculation requires the inclusion of more mechanisms and realistic conditions. Although the process of unraveling the mystery of arc constriction will take much additional study, additional insight and observations can still be made based on previous studies and their steady solutions to help construct future research efforts.

As discussed in the introduction, most theoretical treatments have concentrated on steady state analysis to provide insight into the subject of arc mode transition. These studies have shown that steady current transfer in plasmas tends to take place along certain pathways which minimize energy input (the Steenbeck Minimum Principle, which stipulates essentially that a current takes the path of least resistance) and that the boundary layer voltage drop reaches a maximum at a certain current density (the point where the differential impedance goes to zero).

For the results presented in this chapter, we again compare boundary layers supporting non-dimensional current densities of 0.4 and 40, respectively. In the lower current case we pointed out that the region was in a state of Joule cooling. In Eskin's

thesis, such regions were shown to lie along the "positive impedance" section of the current-voltage characteristic. This basically means that in this current regime, increasing the current density would require an increase in the voltage supplied to the boundary layer. However, in the negative impedance current regime, where the boundary layer is in the state of Joule heating, the opposite is true due to the large numbers of charged particles being produced. This can simply be thought of as the result of an overall increase in conductivity; because there are more charged particles to carry the current, the voltage needed to transfer the current decreases. This line of reasoning cannot be used in describing the regime of positive impedance, however, because of the fact that the concept of "conductivity" really only applies to a simple uniform plasma where the current and field both act in the same direction. For the Joule cooling cases, the current and field flow in opposite directions from each other.

It is possible that these distinctions between the low and high current cases will cause planar perturbations to interact differently with the steady boundary layer. From Figs. 5.5 and 5.9, we find that the electric field perturbation is about 180 degrees out of phase with the number density. For the higher current case, $\bar{J}$ =40, where the boundary layer is characterized by Joule heating, this means that the increase in the electron number density due to the perturbation is coupled with a decrease in the electric field. This corresponds to an increase in conductivity and decrease in the potential in the region which, from the above reasoning, could be interpreted as a possible transition mechanism from a diffuse attachment, higher voltage mode to a constricted attachment, lower voltage mode. For the lower current case, the increase in electron number density again corresponds to a decrease in electric field. However, for this case, the background electric field is negative, which signifies that the overall field would become more negative. The potential of the layer would hence increase as the charged particles are pushed with more force away from the anode. Heuristically, it seems unlikely that such perturbations would result in arc constriction under these conditions.

The above speculation can only be confirmed or disproved with the use of a more general model which takes into account nonlinearity, electrostatic fields, and two-dimensionality. In the present analysis there is no way to analyze the behavior of the perturbations beyond their initial growth phase.

5.6 The role of convection on stability

As discussed in the introduction, bulk fluid convection has been experimentally shown to act as a stabilizing mechanism [12]. As a result, convection may play a significant role in the stabilization of the arc in arcjet thrusters, as well as other plasma devices. In the previous steady state analyses, it was shown that convection reduces the ionization rate requirements in the electric boundary layer by contributing an additional flux of charged particles [10] and hence has an impact on the electric field and voltage characteristics. These observations may help to explain the stabilizing effect of bulk fluid motion, since it is hypothesized in this study that the strength of the instability depends on the net ionization rate and electrical character of the boundary layer.

Chapter 6. Conclusions and Recommendations

The model presented in this thesis represents a fundamental approach to identifying and understanding some of the principal mechanisms responsible for arc mode transition and breakdown. The results of the model provide initial insight into this process as well as a solid foundation to base more detailed analyses on. This chapter summarizes the results of the study, relates the findings to the previous studies done on the subject, and provides suggestions for future studies on arc stability.

6.1. Summary

Our stated objective for this study was to model the time dependent response of small oscillating disturbances in the near-anode region and to identify mechanisms which affect the growth or decay of these disturbances. To this end we began with the calculation of the steady state characteristics of the near-anode region for a current carrying plasma, an approach found in many more recent studies. The set of conditions we chose to model were based on the approximate conditions (based on previous numerical simulations of arcjets) found in the near-anode current attachment region in arcjet thrusters. Many simplifications, such as treating transport and reaction coefficients as constant and ignoring secondary species, were made. Hypothesizing that mode transition is a transient phenomenon, we formulated a stability analysis based on small perturbations in the plasma properties with a sinusoidal time dependence. Assumptions were again made to simplify the stability analysis, the most important one being the modeling of the anode and perturbations with a planar geometry.

To better obtain an understanding of the results we anticipated with our analysis, we paused briefly to perform an analysis based on an unphysical assumption - that of a uniform underdense plasma. By using this simplification we again significantly reduced the mathematical complexity of the analysis, while gaining important insight into the process of interpretating the results. More specifically, we were able to more simply

familiarize ourselves with the concepts of phase and amplitude and how they helped explain the stability characteristics of the calculated modes. We were also able to begin to identify the roles of many mechanisms such as Joule heating, ionization, and conduction on the growth or decay rates of the perturbations. Classifications were given to the modes which resulted from the analysis; an example of this was the "ion" mode, which we found to be a stable mode where ion motion dominated the perturbation characteristics. Finally, we were able to gain additional insight into how basic properties such as bulk temperature, pressure, and the gas type could influence stability.

The final analysis of this thesis was that of the non-uniform case, which took into account the effect of the gradients inherent to the electric boundary layer on arc stability. From this analysis we found that the model was not able to define a specific demarcation point between stable and unstable conditions. However, the influence of specific mechanisms on the stability characteristics of the model became more clear. It was seen for a boundary layer characterized by Joule heating, significant ionization and elevated electron temperature that an unstable mode existed which was best described by runaway charged particle production. An unstable mode was also found in a very low current boundary layer case, though upon closer examination important differences in character from the higher current case were found. This low current instability was described as a "flux" instability, where growth in the charged particle density was the result of a flux imbalance which redistributed the existing charged particles, rather than a significant production of new particles. The effects of these differences on the actual process of arc transition was speculated on and the verification left to future study. In addition, modes which were stable were also identified and examined to help explain their stability characteristics.

6.2. Comparisons to previous studies

We recall that many studies which involved vacuum arc stability found that anode vaporization was a significant factor in mode transition. It was hypothesized that this vaporization resulted in a significant number of ionizable neutral particles, which then

provided a starting point for the transition to an anode spot. Because of this, factors which are important to anode vaporization - anode material, geometry and heat flux into the anode - were identified as having a strong influence on critical current densities. In the higher pressure arcs we are interested in, the number density of the neutral species is assumed to be fixed parameter. However, we found in our model that significant ionization is also an important mechanism for arc instability. It is also interesting to note that the voltage, number density, and temperature fluctuations we would expect to see in the higher pressure cases have been observed in vacuum arc transition, implying that similarities between the two pressure regimes exist.

In our review of experimental high pressure arc studies, we found a common thread that bulk convection had a significant role in maintaining a stable, diffuse arc. Meeks predicted in her numerical model a transition between diffusion-dominated and convection-dominated behavior at a certain bulk fluid flow velocities. She found that operating a diffuse arc under convection-dominated conditions reduced the tendency of the plasma to ionize in the boundary layer region, which we have found to change the character of the perturbations. Because the model presented here neglects convection, we believe that it captures and reflects much of the important qualitative behavior of real diffuse arcs in diffusion-dominated conditions.

6.3. Future directions for study

We believe that the phenomenon of anode spot formation is inherently multi-dimensional; therefore the addition of at least a radial dimension to the model would enhance its ability to more accurately capture the transition process. In addition, non-linear effects will surely become important as the amplitude of the perturbations grow, and should investigated in future studies. To better understand the anode-plasma interaction's effect on stability, more realistic boundary conditions which take into account the various reaction mechanisms and phenomena occuring at the anode would provide improved coupling between the plasma and the electrode. Specifically,

including the sheath would clarify the behavior of the perturbations in non-neutral regions.

The inclusion of convection into the steady state profiles would better relate the modeling work to the previously discussed experimental observations. A parametric study on the effects of varying background pressure, temperature, and gas types would provide better understanding of the current model's capabilities. And finally, the possible effects of an externally applied or internally generated magnetic field, which some researchers believe to have a stabilizing influence, could be incorporated into a newer multi-dimensional model.

References

1. Spores, R.A., Birkan, R., Cohen, R., and R. Einhorn, "The Air Force Electric Propulsion Program," AIAA 95-2378, 31st Joint Propulsion Conference, San Diego, CA, July 1995.

2. Curran, F.M., and L.W. Callahan, "The NASA On-Board Propulsion Program," AIAA 95-2379, 31st Joint Propulsion Conference, San Diego, CA, July 1995.

3. Miller, S.A., and M. Martinez-Sanchez, "Nonequilibrium Numerical Simulation of Radiation-Cooled Arcjet Thrusters, IEPC-93-218, 23rd International Electric Propulsion Conference, September, 1993.

4. Megli, T.W., Krier, H, and R.L. Burton, "A Plasmadynamics Model for Nonequilibrium Processes in N_2/H_2 Arcjets," AIAA-95-1961, 26th AIAA Plasmadynamics and Lasers Conference, June, 1995.

5. Butler, G.W., King, D.Q., "Numerical Modeling of Arcjet Performance," AIAA 21st Fluid Dynamics, Plasma Dynamics and Lasers Conference, Seattle, WA, June 18-20, 1990.

6. Rhodes, R., and D. Keefer, "Modeling Arcjet Space Thrusters," AIAA 91-1994, AIAA 27th Joint Propulsion Conference, June, 1991, Sacramento, CA.

7. Jahn, R.G., *Physics of Electric Propulsion* (McGraw-Hill, Inc., New York)

8. Loh, M.H., and M.A. Cappelli, "Supersonic DC-arcjet Plasma at Subtorr Pressures as a Medium for Diamond Film Synthesis," AIAA-92-3534, 28th Joint Propulsion Conference, July, 1992.

9. Self, S.A., and L.D. Eskin, "The Electrical Boundary Layer and Current Transfer Between a Thermal Plasma and a Plane Electrode," HTGL Report Number T-290, Mechanical Engineering, Stanford University, 1993.

10. Cappelli, M.A., "The Non-Equilibrium Region of an Electrode in Contact with a Flowing Thermal Plasma," IEEE Trans. Plasma Sciences **21**, pp. 194-201, 1993.

11. Meeks, E., "Modeling the Boundary-Layer Interactions Between Weakly Ionized Plasmas and Cooled, Planar Electrodes in Stagnation-Point Flows," HTGL Report Number T-293, Mechanical Engineering, Stanford University, 1993.

12. Sanders, N., Etemadi, K., Hsu, K.C., and E. Pfender, "Studies of the Anode Region of a High-Intensity Argon Arc," J. Apply. Phys. 53(6), June 1982, pp. 4136-4145.

88

13. Miller, H.C., "A Review of Anode Phenomena in Vacuum Arcs," IEEE Trans. Plasma Science, Vol. PS-13, No. 5, Oct. 1985, pp. 242-252.

14. Wang, Y., and G.C. Damstra, "Noise Arc Voltage and Dynamic Constriction of High-Current Vacuum Arcs," Journal of Physics D: Applied Physics, Dec. 14, 1991, pp. 2179-2188.

15. Wieckert, C., and W. Egli, "Theoretical Analysis of the Current and Energy Flow to the Anode in the Diffuse Vacuum Arc," IEEE Trans. Plasma Science, Vol 17, No. 5, pp 649-652, 1989.

16. Barinov, V.N., and A.V. Smirnov, "Relationship Between Electrode Phenomena in vacuum arcs," *Phys. And Chem. Mater. Treat.*, vol 18, pp64-66, 1984.

17. Rich, J.A., Prescott, L.E., and J.D. Cobine, "Anode Phenomena in Metal-Vapor Arcs at High Currents," Journal of Applied Physics, Vol. 42, Feb. 1971, pp. 587-601.

18. Ecker, G., "Anode Spot Instability: I. The Homogeneous Short Gap Instability," IEEE Trans. Plasma Science, Vol. PS-2, Sept. 1974, pp. 130-146.

19. Kimblin, C.W., "Anode Phenomena in Vacuum and Atmospheric Pressure Arcs," IEEE Trans. Plasma Science, Vol. PS-2, Dec. 1974, pp. 310-319.

20. Paik, S., Huang, P.C., Heberlein, J., and E. Pfender, "Determination of the Arc-Root Position in a DC Plasma Torch," Plasma Chemistry and Plasma Processing, Vol 13, No. 3, pp. 379-397, 1993.

21. Okazaki, K., Mori, Y., Hijikata, K., and K. Ohtake, "Electrothermal Instability in the Seeded Combustion Gas Boundary Layer near Cold Electrodes," AIAA Journal, Vol. 16, No. 4, pp. 334-340, 1978.

22. Okazaki, K., Mori, Y., Ohtake, K., and K. Hijikata, "Analysis of the Seeded Combustion Gas Boundary Layer Near a Cold Electrode," AIAA Journal, Vol. 15, No. 12, pp. 1778-1784, 1977.

23. Hinnov, E., and J.G. Hirschberg, "Electron-ion Recombination in Dense Plasmas,", Phys. Rev. **125**, 1962, p. 795.

24. Mitchner, M., and C.H. Kruger, Partially Ionized Gases (John Wiley and Sons, New York), 1974, p. 52.

25. Grcar, J.F., "The Twopnt Program for Boundary Value Problems," Sandia National Laboratories Report SAND91-8230, 1991.